Photoacoustics 32 (2023) 100538

Contents lists available at ScienceDirect

Photoacoustics

journal homepage: www.elsevier.com/locate/pacs

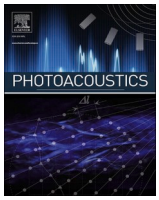

Development and characterization of transfontanelle photoacoustic imaging system for detection of intracranial hemorrhages and measurement of brain oxygenation: *Ex-vivo*

Rayyan Manwar [a,1], Karl Kratkiewicz [b,1], Sadreddin Mahmoodkalayeh [c], Ali Hariri [d], Christos Papadelis [e,f], Anne Hansen [g], De-Ann M. Pillers [h], Juri Gelovani [i,j,k], Kamran Avanaki [a,h,l,*]

[a] *University of Illinois at Chicago, Department of Biomedical Engineering, Chicago, IL, United States*
[b] *Barbara Ann Karmanos Cancer Institute, Detroit, MI, United States*
[c] *Department of Physics, Shahid Beheshti University, Tehran, Iran*
[d] *Department of Nanoengineering, University of California, San Diego, CA, United States*
[e] *Jane and John Justin Neurosciences Center, Cook Children's Health Care System, Fort Worth, TX, United States*
[f] *Department of Bioengineering, University of Texas at Arlington, Arlington, TX, United States*
[g] *Department of Medicine, Boston Children's Hospital, Harvard Medical School, Boston, MA, United States*
[h] *Department of Pediatrics, UI Health Children's Hospital of the University of Illinois at Chicago, Chicago, IL, United States*
[i] *College of Medicine and Health Sciences, United Arab Emirates University, Al Ain, Abu Dhabi, UAE*
[j] *Department of Biomedical Engineering, College of Engineering and School of Medicine, Wayne State University, Detroit, MI 48201, United States*
[k] *Dept. Radiology, Siriraj Hospital, Mahidol University, Bangkok 10700, Thailand*
[l] *Department of Dermatology, University of Illinois at Chicago, Chicago, IL, United States*

ARTICLE INFO

Keywords:
Transfontanelle
Photoacoustic imaging
Neonates
Oxygenation
Hemorrhage

ABSTRACT

We have developed and optimized an imaging system to study and improve the detection of brain hemorrhage and to quantify oxygenation. Since this system is intended to be used for brain imaging in neonates through the skull opening, i.e., fontanelle, we called it, Transfontanelle Photoacoustic Imaging (TFPAI) system. The system is optimized in terms of optical and acoustic designs, thermal safety, and mechanical stability. The lower limit of quantification of TFPAI to detect the location of hemorrhage and its size is evaluated using in-vitro and *ex-vivo* experiments. The capability of TFPAI in measuring the tissue oxygenation and detection of vasogenic edema due to brain blood barrier disruption are demonstrated. The results obtained from our experimental evaluations strongly suggest the potential utility of TFPAI, as a portable imaging modality in the neonatal intensive care unit. Confirmation of these findings in-vivo could facilitate the translation of this promising technology to the clinic.

1. Introduction

Intracranial hemorrhages (ICHs) occur at a rate of approximately 3.5 per 1000 live births, and represent the most common birth complication in newborns [1,2]. ICHs are associated with prolonged or precipitous delivery, vaginal breech delivery, instrumental delivery, use of forceps or vacuum extraction, and primiparity or extreme multiparity [3–12]. Neonates with low gestational age and/or low birthweight (<1500 g) are at high risk for ICH [12] and ischemic brain injuries due to immature vascular, cellular, and anatomical features of the developing brain. During the past few decades, improvements in medical interventions have significantly increased the survival of low gestational age and low birthweight infants, while the potential number of infants with ICH has also increased [13–16]. Moreover, many sub-clinical cases that may not manifest by obvious neurological deficit symptoms remain undiagnosed due to limitations of current diagnostic imaging technologies. The extent of brain injury is dependent on severity and location of the ICH [17,18]. Different types of ICH and their locations are depicted in Fig. 1. Ultimately, a large portion of survivors of neonatal ICH exhibit various degrees of cognitive dysfunctions requiring special education and care

* Corresponding author at: University of Illinois at Chicago, Department of Biomedical Engineering, Chicago, IL, United States.
E-mail address: avanaki@uic.edu (K. Avanaki).
[1] *Authors contributed equally*

https://doi.org/10.1016/j.pacs.2023.100538
Received 28 October 2022; Received in revised form 28 June 2023; Accepted 19 July 2023
Available online 27 July 2023
2213-5979/© 2023 Published by Elsevier GmbH. This is an open access article under the CC BY-NC-ND license (http://creativecommons.org/licenses/by-nc-nd/4.0/).

[19,20]. Therefore, accurate, early detection, classification, and diagnosis of ICH is essential for selection of optimal treatments and prognostication [21–23].

Transfontanelle ultrasound imaging (TFUSI) is the current standard of care diagnostic modality for detection of grades III-IV intraventricular hemorrhage (IVH) [24] (or brain hemorrhages larger than 5 mm) with sensitivity of nearly 100% and specificity of 93.3% [25]. TFUSI can detect large sub-ependymal, intracerebral, subdural, and epidural hematomas, which are usually accompanied by clinical symptoms of neurological deficit [26,27]. However, TFUSI has a low sensitivity and even lower specificity (i.e., 0–5%) for detection of hemorrhages < 5 mm, IVHs of grades I-II, and small cerebral or extra-axial hemorrhages [25,28–31]. Hence, the TFUSI outcomes can be inconclusive during the first week after birth. Therefore, additional US scans are required in the second or third week of life to follow up with any hemorrhagic progression that may be detected, and the possible onset of a Grade IV periventricular hemorrhage (PVH) and/or white matter injury. The frequency of these scans is determined based on the severity of the hemorrhage [32,33]. TFUSI has limited sensitivity and specificity for the detection of subarachnoid hemorrhage (SAH) (without obvious blood clots in the normal-size brain ventricles and cisterns), especially SAH with low-concentration blood in CSF, i.e., $< 10\%$ [13,25]. Also, TFUSI is unable to detect vasogenic edema following hemorrhage or ischemia/reperfusion injury [34].

Although definitive diagnosis of SAH can only be made by the detection of blood in CSF obtained by a lumbar puncture, it is not used as a standard of care in infants due to invasive nature, traumatism, and potential complications. In contrast, magnetic resonance imaging (MRI) and computed tomography (CT) [35] have high sensitivity and specificity for detecting brain hemorrhages. However, they are not used as frontline modalities for routine screening of preterm infants, because routine MRI of the brain takes a long time to set up and conduct the study (~1 h), and CT uses ionizing radiation. Imaging procedures using modalities require transporting clinically unstable newborns out of the Neonatal Intensive Care Unit (NICU), in most cases requiring sedation that is associated with risks (i.e. respiratory depression, hypotension, or hemodynamic changes [36]), and have a relatively high cost per procedure. Small MRI machines, which have been installed and tested in a few NICUs, are expensive and still require sedation during imaging [37]. Therefore, portable MRI units have not been widely adopted in neonatal clinics. Near-infrared spectroscopy (NIRS) can potentially assist clinicians in assessing functional changes in cerebral perfusion and oxygenation [38–40], but it has a poor spatial resolution, especially for the small neonate head, and poor penetration depth, both of which limit its use for cortical mapping [41].

Photoacoustic imaging (PAI) is a promising technique that enables the non-invasive visualization of structural, functional, and molecular changes in organs and tissues [42–44]. PAI combines the technological advances of both optical and acoustic imaging (i.e., the high intrinsic contrast of optical imaging and the spatial resolution of ultrasound (US) imaging) [45–51]. In PAI, nanosecond laser pulses illuminate the tissue at the wavelengths that are absorbed by the endogenous chromophores, e.g., oxy-hemoglobin (HbO_2) and deoxy-hemoglobin (Hb), or by the administered contrast agents [52,53]. The photon absorption causes a transient temperature change which leads to a thermal expansion of photon-absorbing tissue compartments, and consequently a localized pressure change, and the resulting acoustic waves are detected by an ultrasonic transducer. PAI of the brain can simultaneously provide high-resolution images of the brain parenchyma, vasculature, and hemodynamics [48,54–57]. Compared to NIRS, the most popular optical imaging modality used in the NICU to estimate cerebral oxygenation and perfusion, PAI has significantly higher spatial resolution and depth sectioning capability [42,58–62].

In this study, we describe the development, optimization, and evaluation of the transfontanelle photoacoustic imaging (TFPAI) system – a sensitive, portable, and safe imaging modality that can improve the detection of ICH in neonates. The lower limit of sensitivity of TFPAI to detect the location of hemorrhage and its size was evaluated by conducting in-vitro and *ex-vivo* studies. The feasibility of TFPAI for measuring tissue oxygenation and detection of vasogenic edema was also demonstrated. The results obtained from these tests are discussed and the clinical potential of TFPAI is considered.

2. Materials and Methods

We first describe the TFPAI system design and development. We outline the optimization of light delivery (Section 2.1.1) and thermal safety (Section 2.1.2); further details are provided in Supplementary Sections S1 and S2. We then explain the TFPAI system assembly (Section 2.2). The experimental designs related to the application of the TFPAI for in-vitro hemorrhage detection (Section 2.3.1), *ex-vivo* hemorrhage detection (Section 2.3.2), oxygen saturation measurement (Section 2.3.3), and vessel rupture and vasogenic edema detection (Section 2.3.4) are explained next.

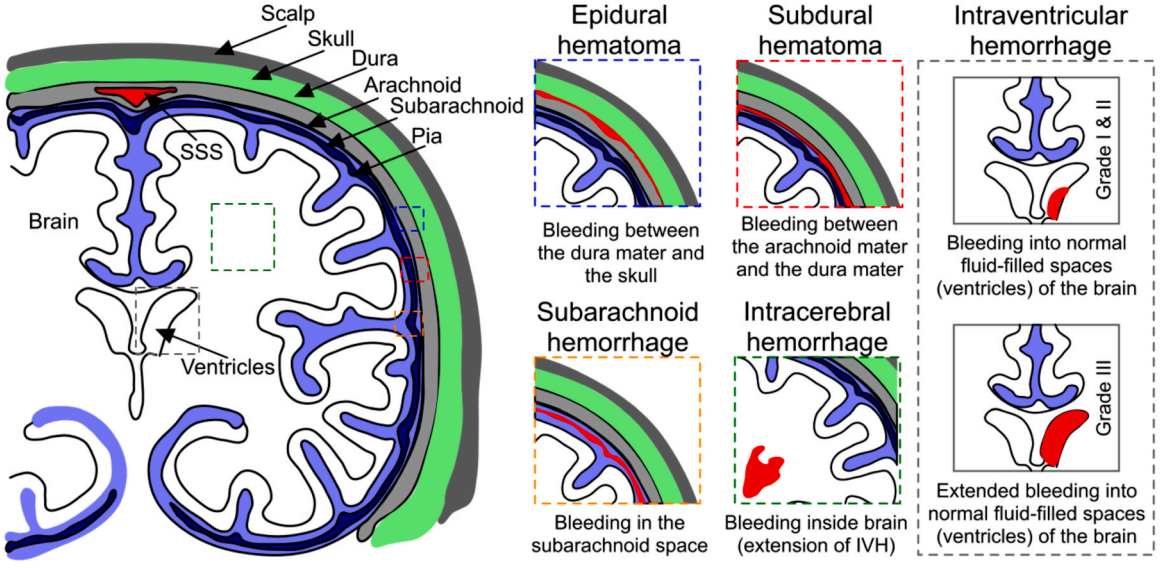

Fig. 1. Different types and locations of intracranial hemorrhages, ICH (epidural, subdural, subarachnoid, intracerebral, intraventricular). IVH: intraventricular hemorrhage; SSS: superior sagittal sinus; Grade IV: extension of IVH into the intracerebral hemorrhage.

2.1. TFPAI system design

2.1.1. Light delivery optimization

The TFPAI system is intended to be placed on the fontanelle and to deliver light with a uniform distribution using a safe laser energy level [63]. A 2D schematic of the TFPAI probe front surface is depicted in Figs. 2 and 3 demonstrates the optical fiber locations relative to the transducer. The diameter of the optical fibers (D), numerical aperture (NA), bending angle (θ), the vertical distance of fiber with the tissue surface (H), distance from the transducer wall to the first row of optical fibers (L) and the arrangement of the optical fibers are the main parameters to be optimized. Monte Carlo simulations using MCX software [64] were used to study the effect of the combination of these parameters on the intensity profile generated on the tissue surface. The number of photons used in the simulation was 10^8. A simulation model with one layer of scalp is used in this study with the following optical properties (absorption coefficient = 0.56 cm^{-1}, scattering coefficient = 250 cm^{-1} and anisotropy factor =0.9 [65]). Parameter values selected for these simulations are as follows: 1) D = 0.5, 1.0, 1.5, 2.0 and 2.5 mm, 2) NA = 0.1, 0.2, 0.3, 0.4 and 0.5, 3) θ = 0, 10, 20, 30, 40, 50, 60 degrees, 4) H = 5, 6, 7, 8, 9 and 10 mm, and 5) L = 5, 6, 7, 8, 9 and 10 mm. After finding intensity profiles for all configurations, we assessed the performance of each configuration to find the best results. To evaluate, we used two criteria: (1) the total light energy inside the fontanelle area and (2) uniformity of the optical energy distribution. Further details of light delivery optimization are given in Supplementary Section S1.

2.1.2. Thermal Safety

To optimize the pulse duration, pulse energy, and repetition rate of the laser used in the TFPAI system, we conducted a thermal safety simulation (to ensure the system is maintained below the tissue heat damage threshold as measured using the cumulative equivalent minutes at 43°C model (CEM43°C)). Optical properties for the simulation (absorption coefficient, scattering coefficient and anisotropy factor) are defined as follows: scalp (μ_a=0.56 cm^{-1}, μ_s=250 cm^{-1} and g=0.9 [65]) and skull (μ_a=0.92 cm^{-1}, μ_s=358 cm^{-1} and g=0.92 [66]). The simulation setup is depicted in Fig. 4. Further details of the thermal safety study are provided in Supplementary Section S2.

2.2. TFPAI experimental system assembly

We used the results of the simulations to implement the optical illumination configuration for the TFPAI system; the schematic of the system is shown in Fig. 2. A Quanta Pro Nd:YAG pump laser (Spectra Physics, USA) with a repetition rate of 10 Hz, and a pulse width of 7 ns was used for illumination (Fig. 2a). A VersaScan optical parametric oscillator (Spectra Physics, USA) was used to tune the wavelength (450–1100 nm). Light exiting the laser passed through a 3D printed parabolic-mirror-like dome with a silvered, inner reflective surface, designed for efficient light delivery. An adjustable, engineered optical diffuser (grit number 240, Thorlabs Inc., USA) and an adjustable achromatic doublet lens (AC254–040-B, Thorlabs, USA) were used for homogenization and focusing of light at the distal end of the optical fiber bundle (Fig. 2b). Light delivery was realized using the optimized fiber arrangement obtained from the MC simulations. As shown in Fig. 2c, the fibers were held in a customized 3D-printed probe tip. 36 wide-bandwidth (500–1300 nm) borosilicate glass optic fibers, each 2 m long (0.5 mm diameter), were used for light delivery. At the distal end, the optical fibers were bundled into a cylindrical holder. One additional optical fiber was diverted to an energy meter (Gentec Integra, USA) to monitor pulse-to-pulse fluctuations for later optical energy normalization. For photoacoustic (PA) signal detection, we have previously evaluated the performance of several transducer arrays (linear arrays: L7–4, L12–5 38 mm and 50 mm, and CL 10–5, and phased arrays: P4–2 and

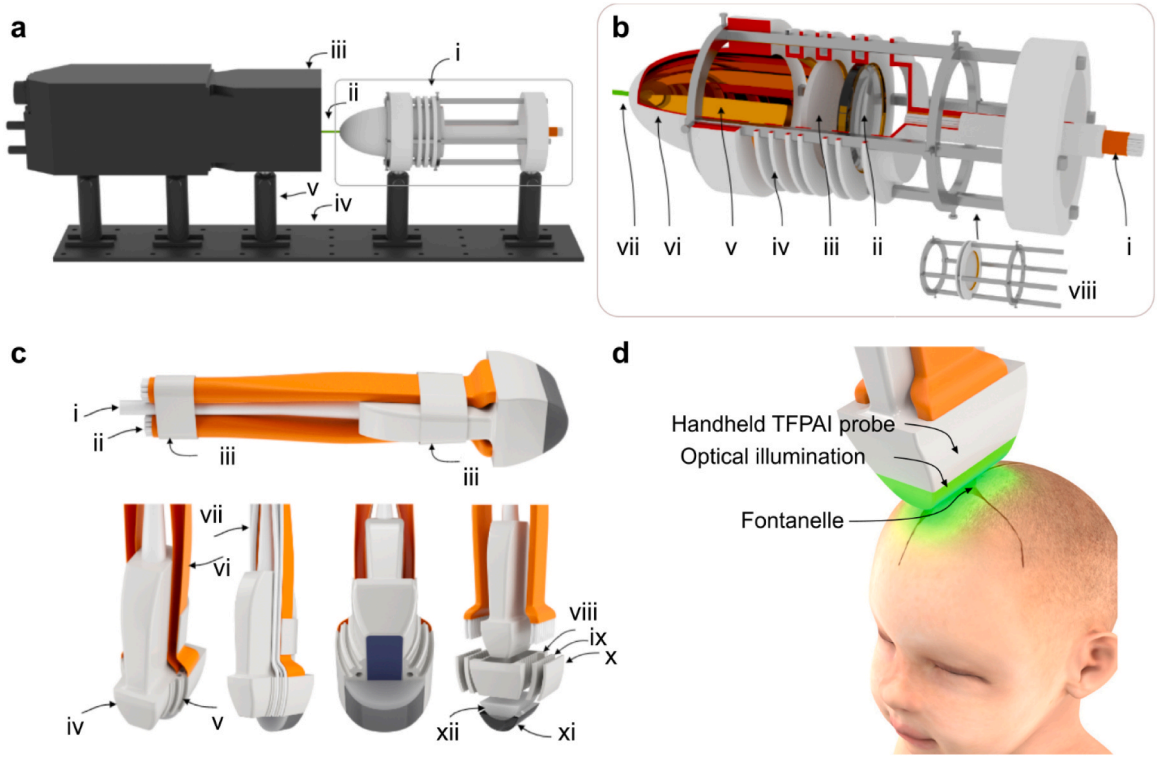

Fig. 2. TFPAI system components. (a) Optical setup of laser light coupling to fiber bundle with (i) laser light coupling optics, (ii) laser light, (iii) laser system head, (iv) optical breadboard, and (v) optical post and post holder. **(b)** Laser light coupling optics cut section view with (i) fiber optic cable bundle, (ii) convex lens, (iii) diffuser, (iv) spacer, (v) parabolic reflector, (vi) thin silver coating, (vii) laser light, and (viii) horizontal cage system. **(c)** TFPAI probe including (i) US data cable, (ii) fiber optic cable bundle, (iii) flexible strap, (iv) linear array transducer, (v) fiber optic cable housing, (vi) fiber optic bundle housing, (vii) fiber optic cable bundle, (viii) main body, (ix) inner fiber optic cable holder, (x) outer fiber optic cable holder, (xi) soft tip, and (xii) Aqualene® coupler. **(d)** Rendering of TFPAI probe in use.

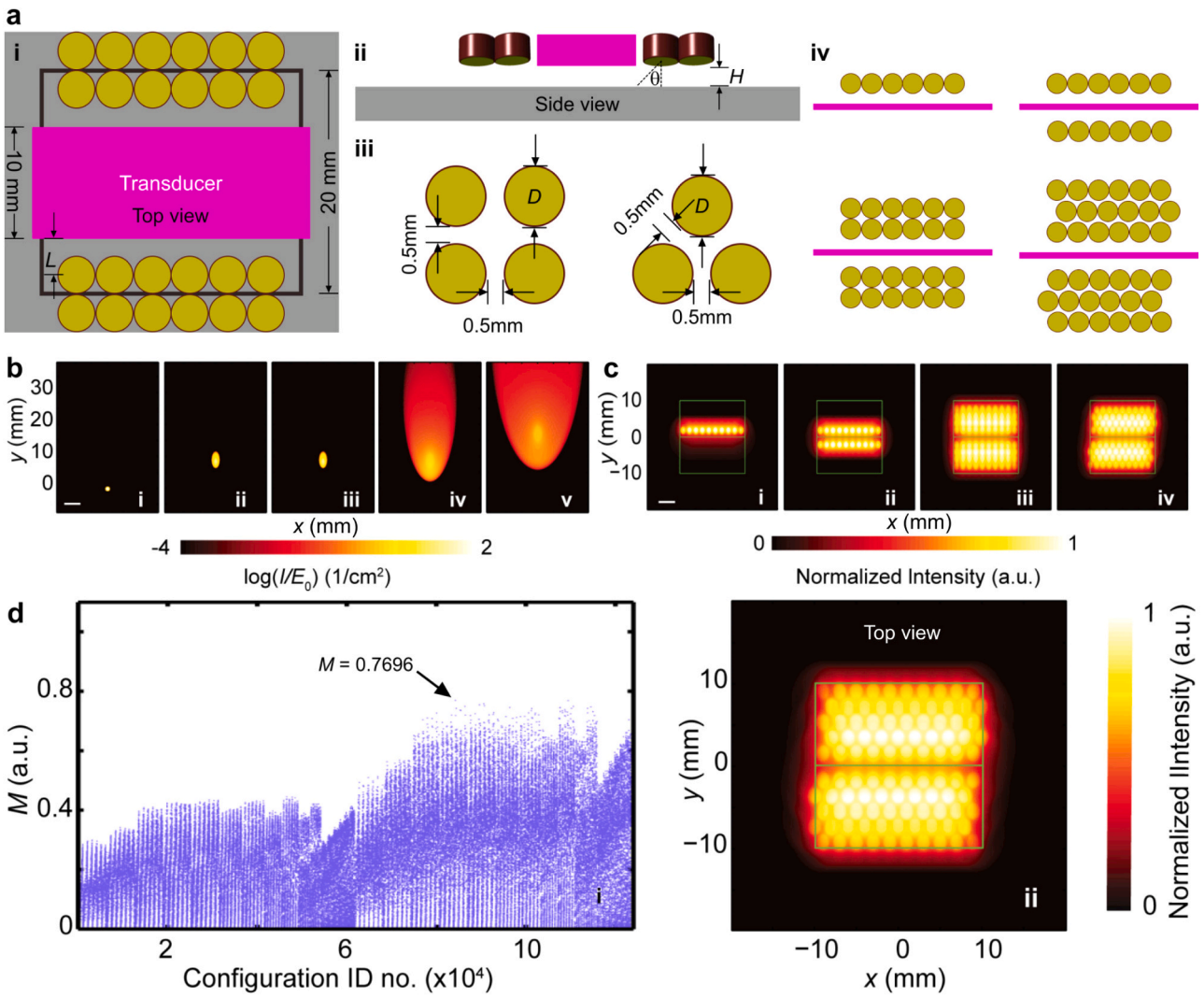

Fig. 3. Simulation studies for optimum light delivery. (a) (i)Top view: an US transducer is placed at the fontanelle center (darker grey outline) and optical fibers (yellow circles) located at the sides act as light sources. Fontanelle is considered as a 20 × 20 mm square (black box). Distance from transducer wall and the first row is *L*, (ii) Side view: the distance between fibers and tissue surface is *H* and bending angle of fibers is *θ*, (iii) fiber diameter, *D*, fiber positioning in a square (left) and honeycomb (right) configurations. The separation between adjacent fibers is 0.5 mm in both cases, (iv) different fiber arrangements: one row at one side (top left), one row on each side (top right), two rows on each side in a square configuration (bottom left) and three rows on each side in a honeycomb configuration (bottom right). **(b)** Effects of changing the parameters of optical fiber on light intensity profile for fiber located at (x,y) = (0,0). Alterations described in (ii-v) are additive. (i) Intensity profile of a single fiber with diameter D = 0.5 mm, numerical aperture (NA) = 0.1, bending angle θ = 0° (perpendicular) and distance from the surface H = 5 mm. (ii) θ = 60°, (iii) D = 2.5 mm, (iv) NA = 0.4 and (v) H = 10 mm. **(c)** Light intensity profiles for different configurations, (i) one row at one side, (ii) one row at each side, (iii) five rows at each side in a square configuration and (iv) in a honeycomb configuration. Green boxes show the fontanelle area, and the middle green line is the US transducer axis. **(d)** (i) Evaluation metric, M (see Supplementary Section S1), for all ~124,000 possible probe configurations considered in this study, (ii) optimized configuration of fiber bundle on the probe side.

P6–3) with the central frequency ranging from 2.5 MHz to 8.5 MHz, which covers the entire spectrum of the transducer arrays typically used for brain imaging. This allows imaging the brain to a depth of 4 cm with an adequate axial resolution [31]. The best-performing US transducer array was the ATL L7–4 (Philips, USA) US probe with 128-elements (element width: 0.25 mm, spacing: 0.3 mm, focal length: 25 mm) and 5 MHz central frequency (bandwidth: 4–7 MHz). PA signal acquisition was performed using a 128-channel, high-frequency, programmable US system (Vantage-128, Verasonics Inc., USA) [67]. To accurately control the movement of the TFPAI probe during measurements, it was placed on a triaxial stage with a clamp. Fully automatic MATLAB code was developed to simultaneously acquire the US and PA signals in A-scan, produce B-mode images and analyze them in real-time [67]. We used a signed-Delay-Multiply-And-Sum (s-DMAS) algorithm for image reconstruction. The design of the s-DMAS algorithm is described in [68]. s-DMAS ensures linearity in the original PA signal response while providing the increased image quality of DMAS [68]. For the transducer-scalp interface, a coupler consisting of a thin layer of Aqualene® filled with water (sack-like) was used.

Aqualene® was chosen as the coupling layer because of its mechanical integrity, chemistry, and the similarities of its acoustic properties to water [69–72]. The optimum thickness for the Aqualene® layer, to meet the required weight tolerance with the least attenuation and best impedance match, was 0.5 mm [73]; these results were obtained from a comprehensive finite element method (FEM) performed for static and dynamic structural analysis. A 3D rendered illustration is depicted in Fig. 2d to demonstrate the application of the TFPAI probe on a neonate's head.

We characterized the TFPAI system resolution in both lateral and axial directions at depths of 0.5–5.0 cm with 0.5 cm steps as follows. We

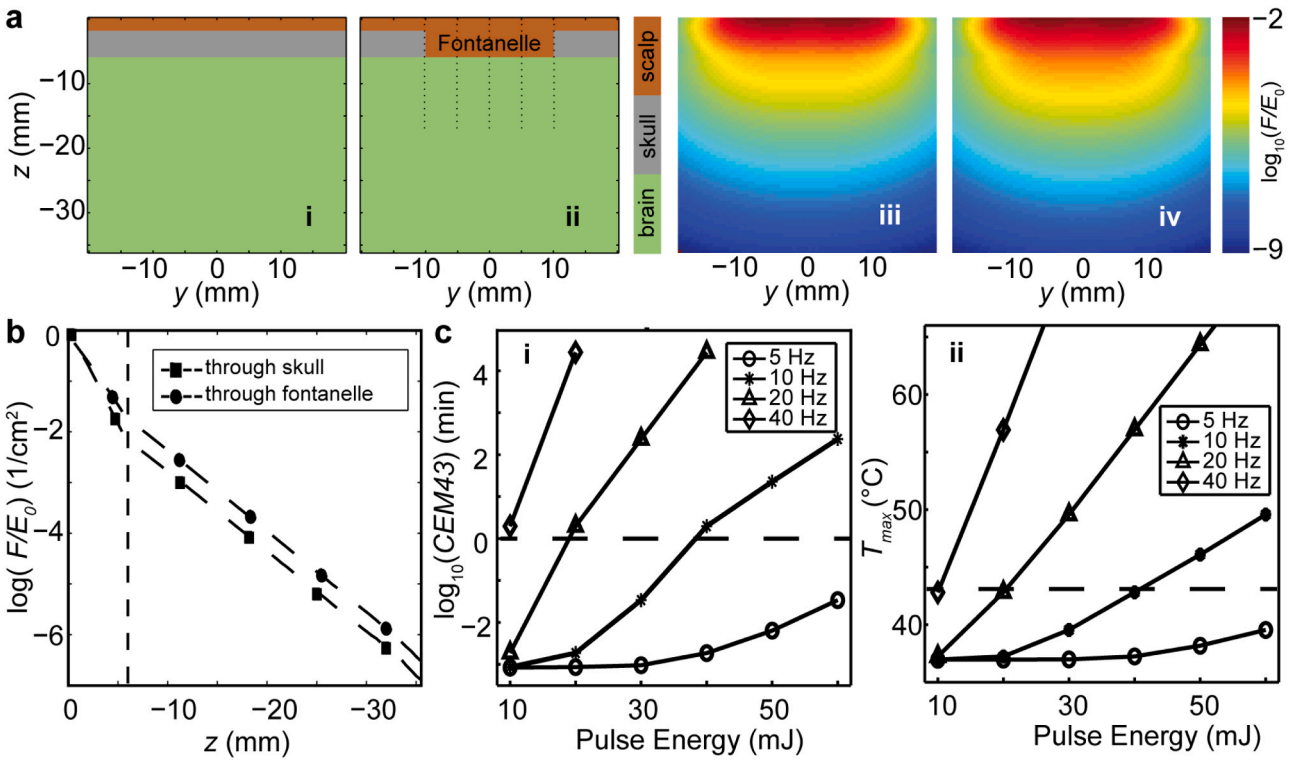

Fig. 4. Optical energy distribution through the fontanelle and evaluation of safety from thermal damage. (a) Fluence inside the tissue and significance of fontanelle, (i) the geometry used for Monte Carlo light simulations with three layers of the scalp (2 mm), skull (4 mm), and brain (20 mm), (ii) the same geometry with a 20 × 20 mm area of scalp to act as fontanelle, (iii) fluence inside the tissue for illumination through the skull and (iv) for trans-fontanelle illumination. **(b)** Normalized fluence decay in log scale (vertical dashed line corresponds to the bottom edge of the skull/ fontanelle as shown in (a-i and ii)). **(c)** Thermal studies: (i) cumulative equivalent minutes at 43 °C (CEM43°C); CEM43°C model gives the equivalent exposure time with the same thermal effect as if the temperature was constant at 43°C, (ii) temperature profile for different configurations of pulse repetition rates and energy levels after illuminating the tissue for 30 s; below the dashed line is considered as a safe choice.

used a phantom made of a human hair (diameter: 54 μm) suspended in deionized water inside an open-top plastic cubic box (see Fig. 5a). A 2D Gaussian was fit to the 1D intensity profile of the PA image of the hair phantom. Next, the full width half maximum (FWHM) was determined from the Gaussian fit (see Fig. 5b-d) [67].

2.3. Experimental designs for application of TFPAI

2.3.1. Preparation of a hemorrhage phantom (In-vitro)

This study was designed to demonstrate the advantage of the TFPAI over conventional US imaging for the detection and assessment of the severity of ICH, by utilizing the innate higher sensitivity of PAI for the detection of blood (hemoglobin). The schematics of the experimental setup are shown in Fig. 6a. A series of phantoms were prepared using 8% gelatin in distilled water that was left to solidify in small cups with a 0.5 cm diameter aluminum rod in their top to mold a small cylindrical opening 0.5–1.0 cm deep. To model the ICH distributed inside the ventricular space, the heparinized sheep blood (Quad Five, USA), at different concentrations, i.e., 0.2%, 0.4%, 0.8%, 1.6%, 3.13%, 6.3%, 12.5%, and 25% (in 1 × phosphate buffered saline) was injected into the openings of the gelatin phantoms (see Fig. 6b). To model the intracerebral hemorrhage, we prepared the gelatin phantoms with different concentrations of sheep blood (i.e., 0.2%, 0.25%, 0.3%, 0.4%, 0.5%, 0.6%, 0.8%, 1%, 1.2%, 1.6%, 3.13%, 6.3%, 12.5% and 25%) mixed with homogenized sheep brain tissue at 2% by wt/vol (Fig. 6c). A thin layer of gelatin was added on top of each phantom (~2 mm) for phantom integrity.

2.3.2. Hemorrhage detection inside the sheep brain (Ex-vivo)

In this *ex-vivo* study, we tested the ability of TFPAI to detect a hemorrhage in an adult sheep brain. The rationale for choosing a sheep model is: 1) the brain is closest in size to a human neonatal brain (especially preterm neonatal brain) and 2) skull anatomy is amenable to relatively easy surgical access [74–76]. Adult sheep do not have a cranial fontanelle (a natural "window" enabling efficient light illumination and US or more precisely PA detection). Therefore, conducting *ex-vivo* studies on a sheep head with a surgically induced cranial window which represents a fontanelle, will produce the most relevant results. Several freshly decapitated sheep heads were purchased from a local slaughterhouse. Initially, hair, fatty tissues and flesh were removed from the top of the head using a scalpel, followed by cleaning the pseudo-fontanelle area, then a hole was drilled into the skull with a circular saw (Fig. 7a(i)) to expose the dura without rupturing it. Chicken skin (representing scalp) was placed over the cranial window to cover the exposed dura mater. In a typical experiment (the experimental setup and its detail are shown in Fig. 7a(ii-iv)), PA and US "before" images were collected of the sheep brain. Next, the blood/brain tissue mixture was injected into the brain (the tip of the needle was guided through US imaging). The air gaps between the chicken skin and dura mater, and the transducer surface and the skin, were filled with US gel (Aquasonic Inc., USA), to ensure the acoustic coupling. Then, a second set of PA and US images ("after") were collected. The PA and US before images were subtracted from the after images and binarized (including only 80% of maximum intensity or more) to identify the hemorrhage area. The rationale for using subtraction to identify injected blood is that *ex-vivo* heads contain blood clots that will generate US and PA signal that is otherwise not distinguishable from the injected, controlled hemorrhage phantoms.

Two sets of experiments were performed: (a) different size hemorrhages were created in the sheep brain by injecting varying quantities of

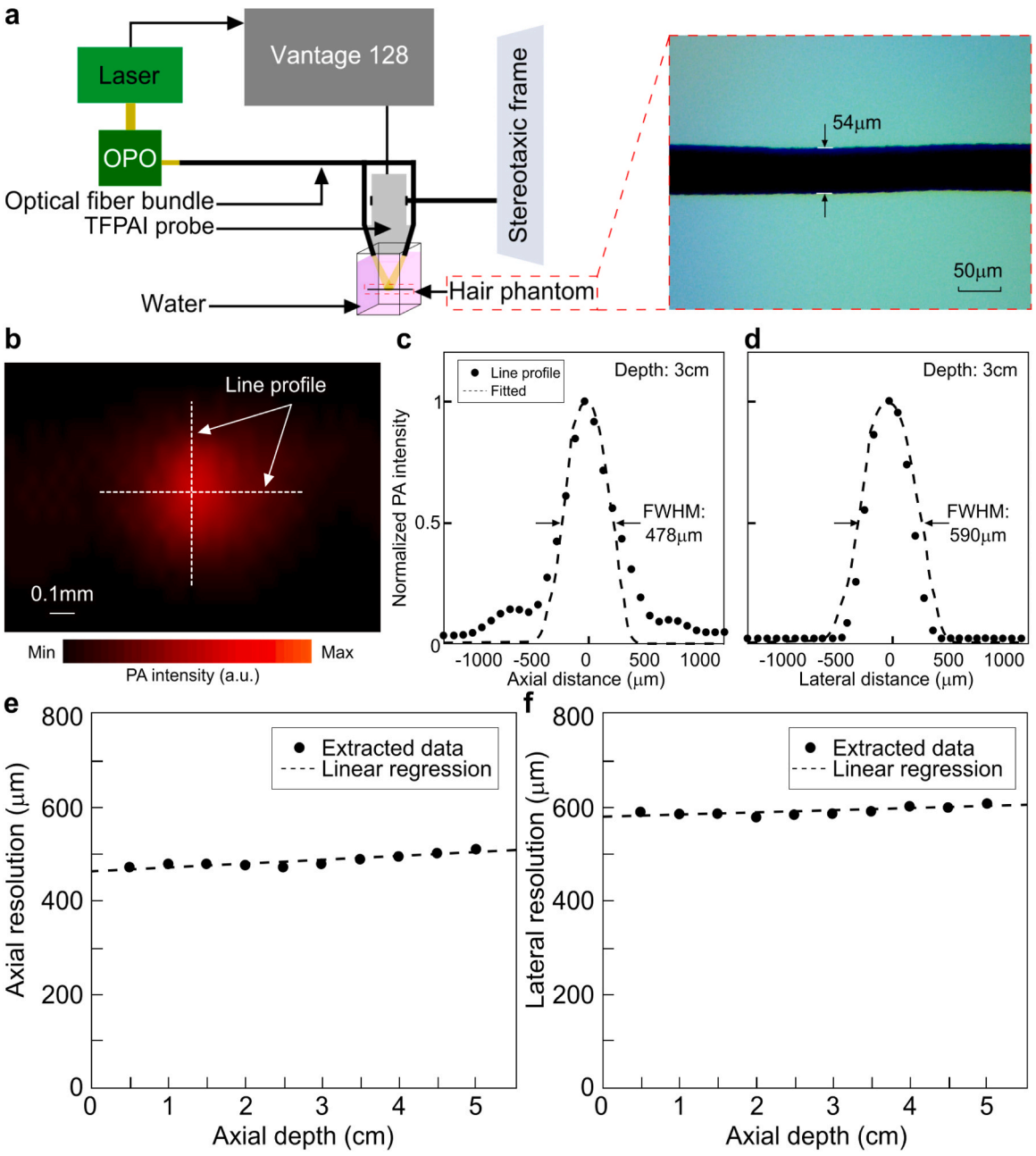

Fig. 5. TFPAI probe resolution as a function depth. (a) Schematic of the experimental setup, including a hair phantom photograph captured by a 4 × objective on a light microscope (SME-F8BH, Amscope, CA, USA). **(b)** PA image of a hair. The dotted line shows the cross section from which the full-width half maximum (FWHM) is calculated. **(c)** 1D intensity profile obtained from the specified cross section. **(d)** 2D Gaussian fit of the intensity profile. **(e)** Axial and **(f)** lateral resolutions versus depth. OPO: optical parametric oscillator.

blood/brain tissue mixture (20 – 100μl, step size of 20 μL) at a depth of approximately 2.5 cm; and (b) same size of hemorrhage (20μl) at depths varying from 0.5 cm to 2.5 cm. To quantify, we have utilized a wavelength-dependent fluence compensation curve which was generated based on the measured optical energy at different depths of a sheep brain tissue, as explained in [47].

2.3.3. *Oxygen saturation measurement*

The impairment of blood flow, with subsequent tissue hypoperfusion and hypoxia (lack of brain oxygenation), can be caused by a hemorrhage or by an ischemic stroke [46]. TFPAI, using at least two wavelengths and spectroscopic analysis, is designed to measure oxygen saturation in the brain vasculature. We have chosen 758 nm (λ_1) where the absorption ratio of deoxy-(Hb) and oxyhemoglobin (HbO_2) has a local peak. According to *Wang* et al. [77,78], this selection will increase the dynamic range of the spectroscopic absorption differences between HbO_2 and Hb and hence improve the accuracy of PA measurements. Using the spectroscopy formula, Eq. (1), [77–81], a value for sO_2 was obtained. At 798 nm (λ_2) wavelength (isosbestic point), $\varepsilon_{HbO_2}^{\lambda_2} = \varepsilon_{HbR}^{\lambda_2}$; therefore, $\Delta\varepsilon_{Hb}^{\lambda_2=798} = 0$. First term in the denominator of the original equation (as shown below) presented in literature is simplified for further calculation.

$$sO_2 = \frac{C_{HbO_2}}{C_{HbO_2} + C_{HbR}} = \frac{\mu_a^{\lambda_2}\varepsilon_{Hb}^{\lambda_1} - \mu_a^{\lambda_1}\varepsilon_{Hb}^{\lambda_2}}{\mu_a^{\lambda_1}\Delta\varepsilon_{Hb}^{\lambda_2} - \mu_a^{\lambda_2}\Delta\varepsilon_{Hb}^{\lambda_1}}$$
$$sO_2 = -\frac{\varepsilon_{Hb}^{758}}{\Delta\varepsilon_{Hb}^{758}} + \frac{\varepsilon_{Hb}^{798}}{\Delta\varepsilon_{Hb}^{758}}\frac{\mu_a^{758}}{\mu_a^{798}}; \Delta\varepsilon_{Hb}^{\lambda_2=798} = 0 \quad (1)$$

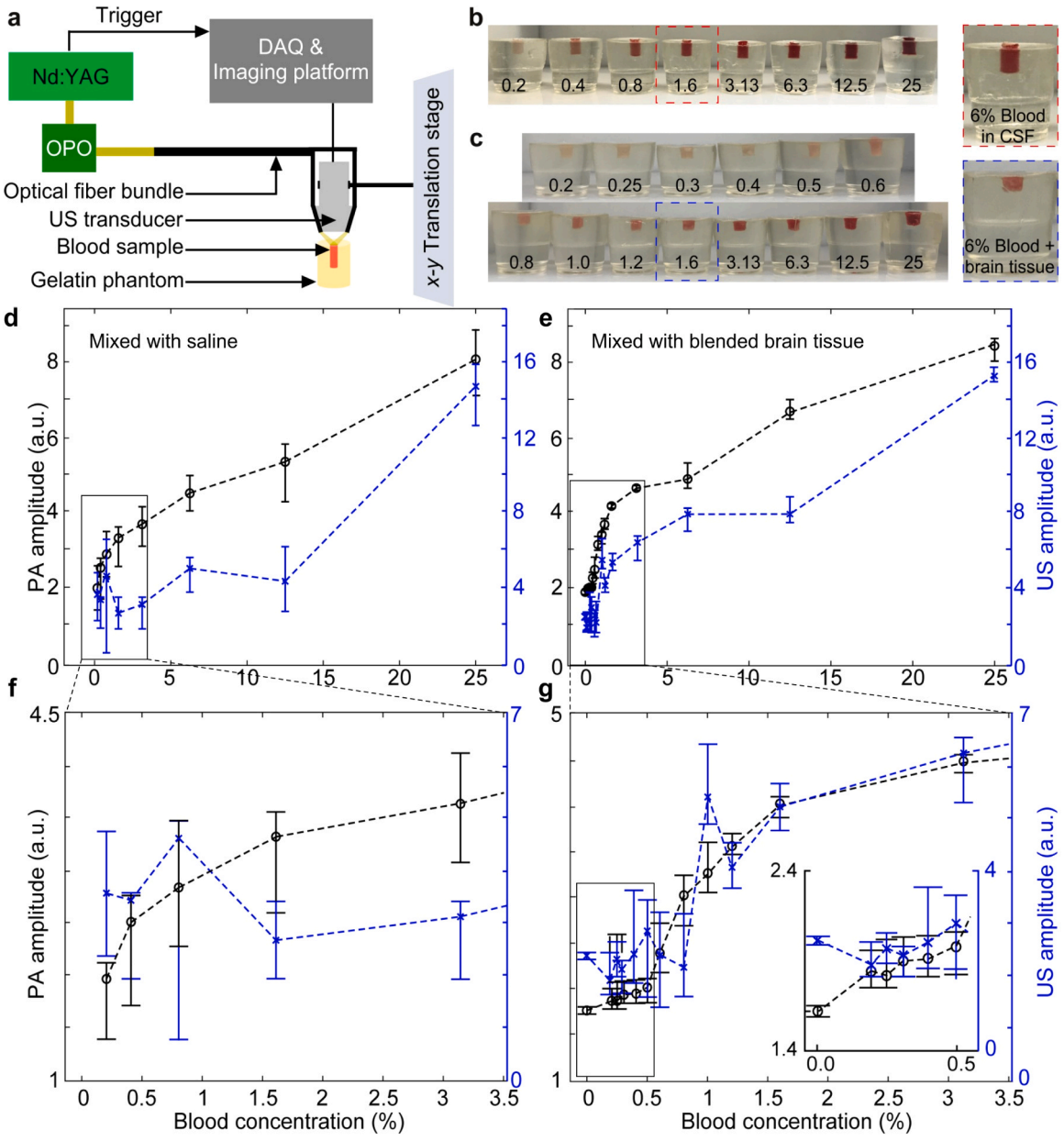

Fig. 6. PA versus US amplitude in measuring the severity of hemorrhages. (a) Schematic of the experimental setup. **(b)** Photograph of heparinized sheep blood sample diluted with saline suspended in gelatin phantom mimicking blood in CSF or early-stage intraventricular hemorrhage, and **(c)** photograph of heparinized sheep blood samples mixed with blended brain tissue in gelatin phantom mimicking intracerebral hemorrhage. **(d)** PA and US signal amplitudes from heparinized sheep blood diluted with saline in gelatin phantom. **(e)** PA and US signal amplitudes from heparinized sheep blood mixed with blended brain tissue in gelatin phantom. **(f** and **g)** Data points in **(d)** and **(e)** at lower concentrations are magnified. The inset in **(g)** is a magnified version of the specified box in **(g)**. OPO: optical parametric oscillator, DAQ: data acquisition, CSF: cerebrospinal fluid.

To confirm the ability of TFPAI to measure the sO_2, we imaged undiluted heparinized sheep blood in a capillary system with varying oxygen saturations (sO_2) and compared the sO_2 measurements derived from the PA signal amplitude to measurements obtained using a blood-gas analyzer (BGA) (Opti CCA-TS, Optimedical, USA). The schematic and actual experimental setup are shown in Fig. 8a and b. We varied the blood oxygen saturation from 62% to 95% to model the hypoxic and normoxic tissue scenarios. As measured by BGA, the sO_2 of fresh blood was 95%, while the sO_2 of blood refrigerated for a few days was only 60%. To achieve different levels of sO_2, the fresh and old refrigerated blood samples were mixed at different proportions without exposing the samples to the atmospheric air. Specifically, the 95% sO_2 blood was imaged, followed by mixing 15 mL of this high sO_2 blood with 5 mL of the 60% sO_2 blood. The resulting mixture was continually mixed with 5 mL of 60% saturated blood until the lowest oxygen saturation (~62%) was achieved. The sO_2 of the blood mixture was stable during imaging and confirmed by measuring the oxygenation level using the BGA before and after the imaging. Blood samples for each saturation level were imaged inside a low concentration of intralipid-10% (1%) at depths of 0.5–5.0 cm in 0.5 cm increments. We recognize this low concentration of intralipid-10% is a less scattering environment than brain tissue. We used this concentration to specifically study the effect of depth and its relation to the focal range of the detection transducer on sO_2 measurements, without the confounding problems of increased attenuation and reduced fluence.

2.3.4. Vessel rupture and vasogenic edema detection using contrast agent

When a vessel ruptures in the brain and bleeds, it not only creates a

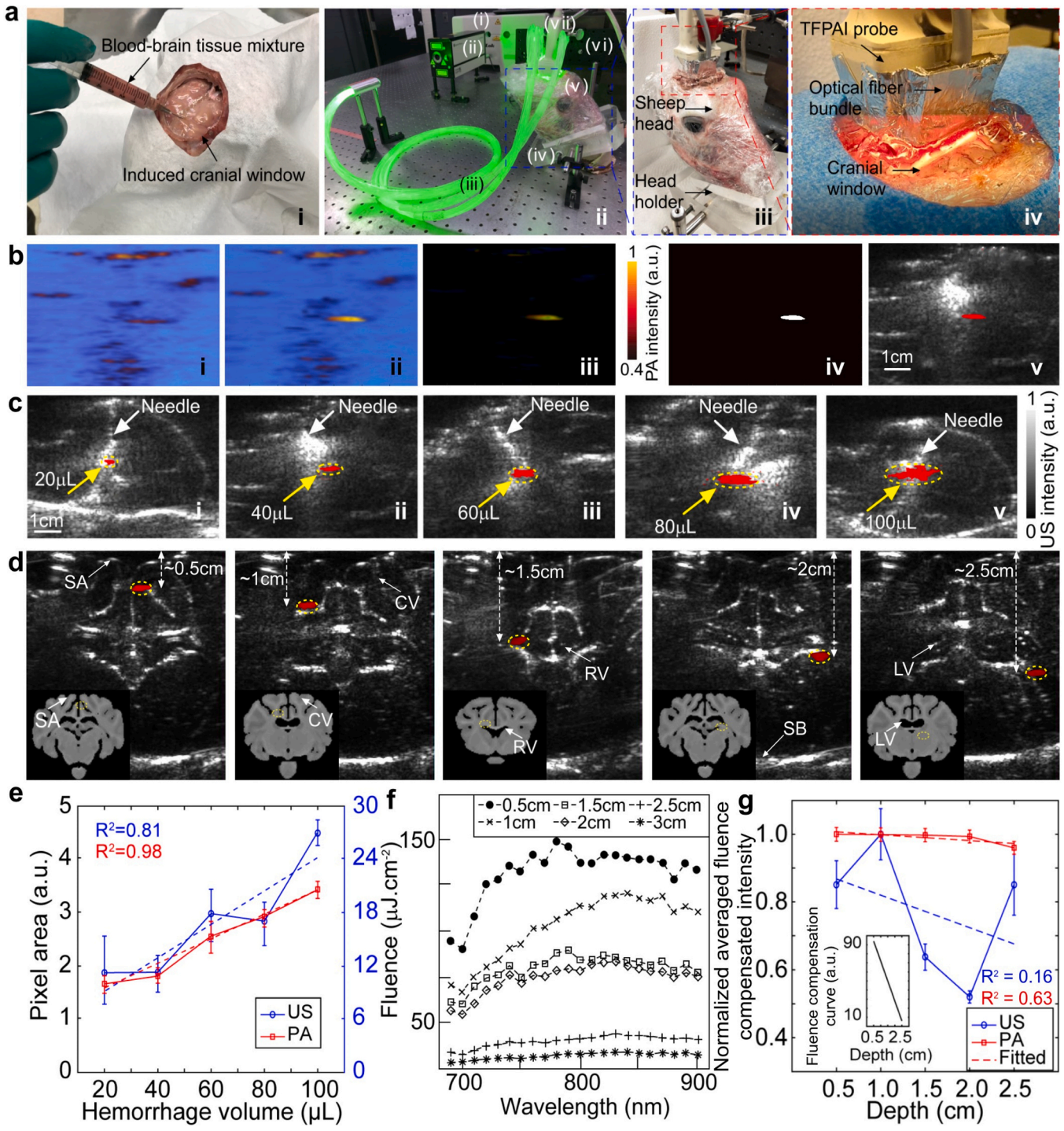

Fig. 7. A feasibility study of TFPAI for detection of intracerebral hemorrhage in an *ex-vivo* model in sheep. (a) (i)The preparation of the *ex-vivo* sheep head included drilling of a 6 cm diameter cranial window in frontal bone and injection of blood-brain tissue mixture, (ii) experimental setup including sheep head, head holder, TFPAI probe, and optical fiber bundle, (iii) sheep head showing probe placement on induced cranial window, (iv) detail of probe with optical fiber bundle and placement at the surgically-created cranial window. **(b)** Hemorrhage detection image processing steps applied on PA images taken from the sheep brain *ex-vivo*, (i) PA image of the sheep brain before blood injection (40 μL), (ii) PA image of the sheep brain after blood injection, (iii) subtraction of the image in (i) from the image in (ii), (iv) binarize the resultant image, (v) overlaid hemorrhagic identified region on the US image. **(c)** The overlaid hemorrhagic area on US images. With increasing volumes of injected blood, the hemorrhagic area has increased. Volumes of blood injected were: (i) 20 μL, (ii) 40 μL, (iii) 60 μL, (iv) 80 μL, (v) 100 μL at 2.5 cm deep inside the brain tissue. **(d)** PA images of injected hemorrhage (20 μL) at different depths: (i) 0.5 cm, (ii) 1.0 cm, (iii) 1.5 cm, (iv) 2.0 cm, and (v) 2.5 cm overlaid on US images. **(e)** Actual pixel area of hemorrhages determined from PA and US images as a function of hemorrhage volume (20, 40, 60, 80, and 100 μL), images acquired at ~2.5 cm depth. **(f)** Measured fluence at different depths of brain tissue (0.5–3.0 cm) as a function of wavelength, ranging from 700 nm to 900 nm. **(g)** Normalized, averaged intensity extracted from US image (blue) and normalized, averaged, fluence-compensated intensity extracted from PA image (red), and corresponding fitted curves demonstrating quantification of the same hemorrhage (20 μL) at different depths. The fluence compensation curve is shown as an inset. SA: subarachnoid, CV: cortical vasculature, RV: right ventricle, LV: left ventricle, SB: skull base.

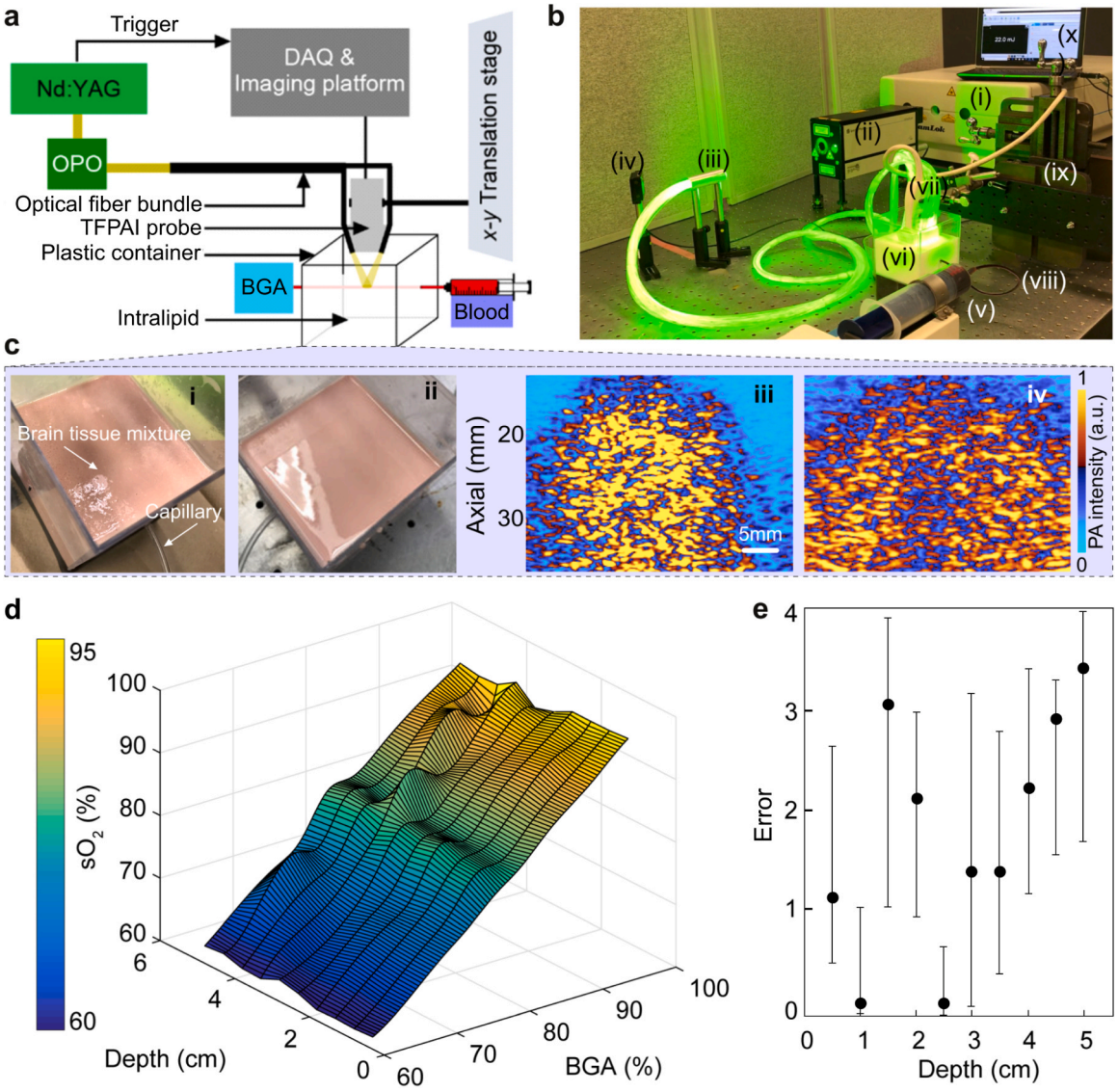

Fig. 8. Oxygen saturation measurement in-vitro. (a) Schematic of the oxygen saturation measurement and validation setup. **(b)** Experimental setup of in-vitro probe characterization. (i) Laser head, (ii) optical parametric oscillator, (iii) fiber bundle, (iv) energy meter (Gentec-EO, Canada), (v) automatic syringe pump, (vi) intralipid solution, (vii) TFPAI probe, (viii) capillary representing vessel, (ix) translation stage, (x) laptop for energy measurement and wavelength switching. **(c)** Homogenized sheep brain tissue was tested for use as a tissue-mimicking environment in in-vitro oxygenation study. Brain tissue mixture (i) whole phantom (initial phase) before removing air bubbles in solution generated from the blending, (ii) whole phantom (after removing bubbles), PA images (iii) before and (iv) after removing air bubbles. **(d)** Oxygen saturation of continuously flowing heparinized sheep blood within the range of 62–95% measured by TFPAI at depths of 0.5–5.0 cm with 0.5 cm increments; compared with and validated by the gold standard BGA measurement results. **(e)** Average error percentage. OPO: optical parametric oscillators, BGA: blood gas analyzer, DAQ: data acquisition.

blood clot but also generates edema (swelling, i.e., the extracellular accumulation of fluid resulting from disruption of the BBB and extravasations of serum proteins). US imaging is rather insensitive [82] to differentiating edema from blood [83,84]. Due to the lack of strong absorbing components in the regions of brain edema, no strong PA signal is generated in these regions either. Methylene Blue (MB) is an FDA-approved contrast agent that binds to plasma proteins and has been used in neonatology for the past several years [85]. It is frequently stated in blood-brain barrier studies that MB binds rapidly, with good affinity to albumin [86,87]. A key criterion for MB dye is that, with a much smaller concentration it remains in the circulation at a constant level for 40 min [87]. Using this contrast agent, quantitative assessments of damage to the blood-brain barrier can be realized. The contrast agent also lights up the edematous regions. Therefore, we investigated the use of MB as a possible exogenous contrast agent for TFPAI to identify the localization of the sites of vascular rupture and brain edema regions.

Vessel Rupture Phantom: The experimental setup is shown in Fig. 9a. An agar-gelatin based bilayer phantom was made to model the rupture in a vessel (Fig. 9b(i)). Steps 1: a 2 cm thick 3% agar solution in a plastic, open-top box was created with two separate cylindrical inclusions. A larger diameter inclusion (4 mm) represented the main vessel and the smaller inclusion (2 mm deep) represented the location where the rupture occurred. A horizontally placed aluminum rod created the larger inclusion, and a vertically placed aluminum rod created the smaller one. Mold release (Smooth-on Inc., USA) was sprayed on the aluminum rods for easy release from agar. Once the agar solution set, an 8% gelatin solution was created to surround the main vessel and left at room temperature to cure. Step 2: After both layers were set, the rods were carefully taken out to avoid any cracks in the phantom layers. Step 3: The smaller inclusion was filled with defibrinated and undiluted sheep blood. Step 4: Next, a slight vacuum was applied to the exterior of the box to pull the blood into the smaller hollow space, or inclusion. Step 5:

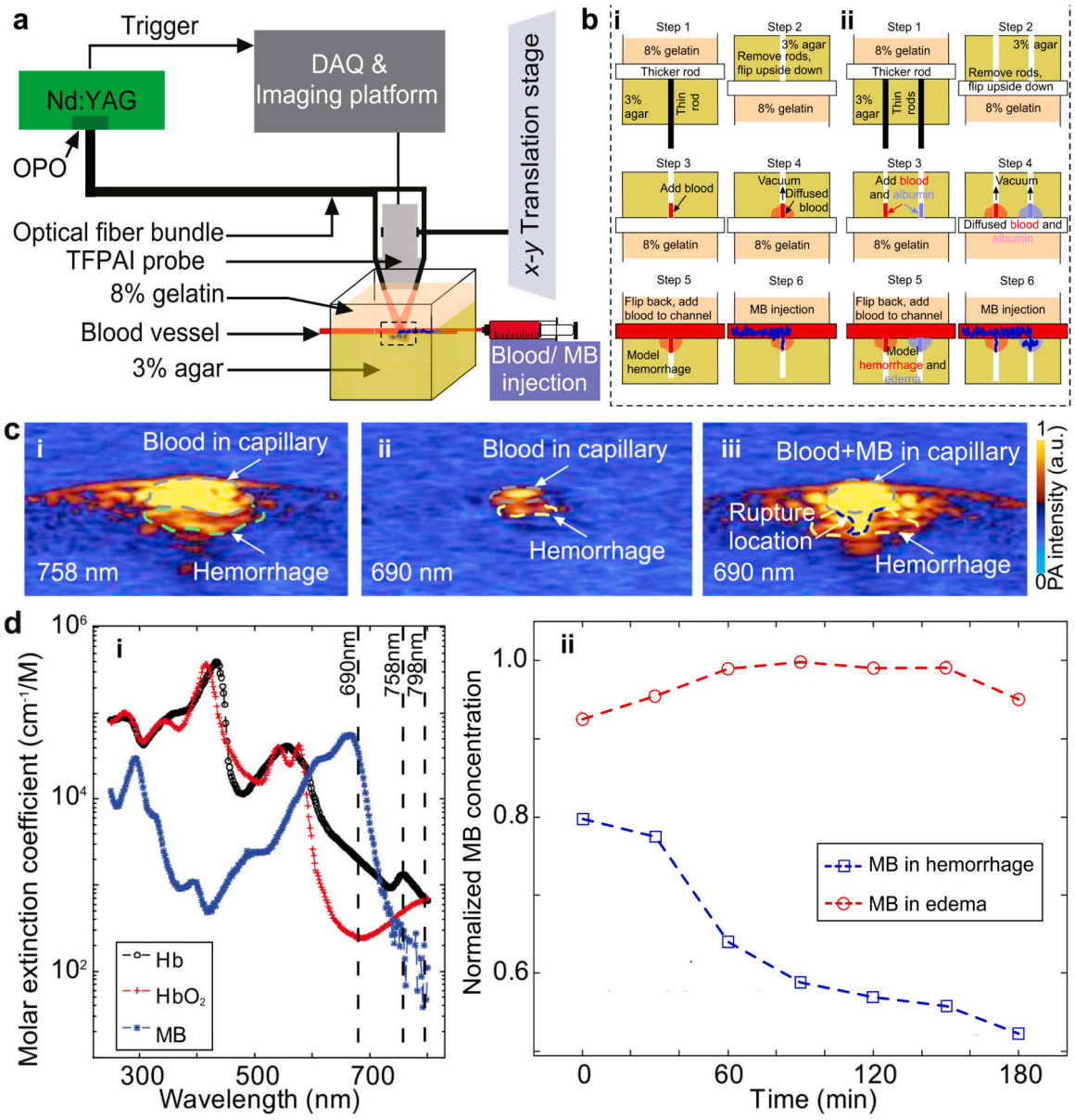

Fig. 9. Validation of TFPAI vessel rupture localization and vasogenic edema detection using MB. (a) Schematic of the experimental setup for imaging the vessel rupture phantom and edema model phantom. **(b)** Steps for creating (i) vessel rupture phantom and (ii) edema model phantom (see Section 2.3.4 for a full description). **(d)** (i) injection of blood in the main vessel and imaged at 758 nm, (ii) reduction in PA image intensity when imaged at 690 nm, (iii) intensity increase in both main vessel and the rupture location due to presence of MB, imaged at 690 nm. The rupture location is annotated. **(e)** (i) Molar extinction coefficients from 250 to 800 nm for MB, Hb, and HbO_2. Dashed lines represent wavelengths used in these experiments, (ii) normalized MB concentrations over time for edema-like inclusion (with albumin) (red) and hemorrhage-like inclusion (no albumin) (blue) calculated through unmixing of Hb and HbO2 from MB [90].

The larger inclusion was filled with heparinized sheep blood. The diffused blood from the smaller hollow space mimics the hemorrhage model. Step 6: For the detection of rupture location, we created a 1 mg/mL MB saline solution, and slowly injected it into the blood-filled main vessel of the gelatin phantom.

Edema Model Phantom: In another experiment (Fig. 9b(ii)), a phantom including an edema model was realized. Step 1: a 2 cm thick 3% agar solution in a plastic, open-top box was created with one larger diameter inclusion (4 mm) representing the main vessel and two smaller inclusions (2 mm deep) representing both a rupture location and an edema location. Step 2: Similar to Step 2 of the Vessel Rupture Phantom method. Step 3: One smaller inclusion space was filled with defibrinated and undiluted sheep blood and the other smaller inclusion was filled with 1 mL egg white, which contains albumin. Step 4: A slight vacuum was applied to the exterior of the box to pull the blood (inclusion #1) or egg white (inclusion #2) into the surrounding space. Step 5: The larger inclusion was filled with heparinized sheep blood. Step 6: For the detection of hemorrhage and edema, we created a 1 mg/mL MB saline solution, and slowly injected it into the blood-filled main vessel of the gelatin phantom where it diffused into both smaller inclusions. We imaged both inclusion locations at three different wavelengths (690, 758 and 798 nm) every 30 min for 3 h. The images were processed pixel-by-pixel using a matrix pseudo-inverse unmixing algorithm to obtain concentration of MB in each inclusion.

3. Results

3.1. TFPAI design optimization: simulation study

3.1.1. Optical energy delivery optimization

The impact of fiber parameters and configurations on optical energy delivery is shown in Fig. 3. The intensity profile of a single fiber with baseline parameter values of diameter $D = 0.5$ mm, $NA = 0.1$, bending angle $\theta = 0^{o}$ (perpendicular), and a distance from the surface $H = 5$ mm is shown in Fig. 3b(i). In Fig. 3b(ii-v), we demonstrate the effect of changing each of the design parameters from baseline, in turn, in an additive fashion (ii) $\theta = 60^{o}$, (iii) $D = 2.5$ mm, (iv) $NA = 0.4$ and (v) $H = 10$ mm. In addition, an optimum arrangement of the fibers was explored. For this, various numbers of rows of identical fibers were placed on either side of the transducer, and the optical intensity profile was computed. In addition to the number of rows, we introduced a parameter L, the distance between the first row and transducer edge; the width of the probe ranged from 10 to 20 mm. Note that the width of the probe did not exceed 4 cm^2 area in any configuration. Fig. 3c(i-iv) demonstrates examples of light-intensity profiles with varying fiber configurations. The green box shows the potential fontanelle area while the center green line indicates the axis of the transducer. Optimization was performed to maximize the value of M where the M value indicates the uniformity and confinement of the intensity profile (for further details, please see Supplementary Section 1 Eq. (1)). The light intensity profile for all permutations of all of the above parameters in both square and honeycomb fashion, amounting to a total number of ~124,000 (configuration ID in Fig. 3d (i)) combinations were obtained. All configurations assumed an equal input energy to the optical fiber bundle.

These results are shown in the scatter plot of Fig. 3d(i). Each configuration ID refers to a specific probe configuration with a known set of parameters. The ID with the highest metric ($M = 0.7696$), that is, greatest homogeneity with highest total illumination to the target, referred to the probe configuration consisting of 4 rows of fibers in a honeycomb pattern, on either side of the transducer with the following parameter combination: D=1.5 mm, $NA = 0.5$, $\theta = 40^{o}$, H=5 mm, and L=5 mm (see Fig. 3d(ii)). This configuration was used for all of the following experiments. Some of the NAs with/without "fiber bending angles" wasted a lot of laser energy because a fraction of the illumination was outside of the fontanelle area, and that decreased M dramatically.

3.1.2. Energy deposition and thermal safety simulation

To demonstrate improved energy deposition through a fontanelle and to confirm that TFPAI will not cause thermal damage to tissues, we simulated energy deposition with a skull and through a fontanelle. We considered two geometries in MCX simulations. Initially, we used a 3-layer slab model with the top layer representing scalp (2 mm), the middle layer – skull (4 mm), and the bottom layer – brain (20 mm), shown in Fig. 4a(i). In the second case, we used the same geometry, except replacing a 20 × 20 mm^2 region of the skull with scalp tissue to simulate a fontanelle, as shown in Fig. 4a(ii). Corresponding fluence maps are depicted in Fig. 4a(iii and iv). Both tissues were illuminated on the surface with the optimized probe configuration described above. Due to lower attenuation, the fluence of light after passing through the fontanelle is 2.4 times higher than the light passing through the skull, see Fig. 4b.

The TFPAI probe was also characterized and optimized from a thermal safety point of view. For thermal calculations, we used readings from a sensor array illustrated with black dots in Fig. 4a(ii).

It is evident that with higher repetition rates the temperature increases very fast even with lower pulse energies, since the tissue has less time to cool down; for instance, with 40 Hz repetition rate even with 10 mJ pulses, a considerable thermal dose is delivered in 30 s [88]. Fig. 4c(i) shows the highest thermal dose received by the tissue calculated based on the CEM43°C model. The dashed line in Fig. 4c(i) corresponds to 1 min of equivalent thermal dose at 43°C. Fig. 4c(ii) shows the maximum temperature rise after 30 s of illumination, which is considered the duration of a typical imaging session. Any configuration that is below the threshold can be considered safe [88]. Based on these simulation models, we selected a 10 Hz laser pulse repetition rate with 30 mJ pulse energy: well within the safety limit.

3.2. TFPAI system characterization

We have experimentally determined the resolution of the TFPAI probe, based on L7–4 US transducer, by imaging the 54 μm cross-section of a human hair. Fig. 5b-d demonstrate the postprocessing steps (see more details in the caption of Fig. 5. As shown in Fig. 5b and c, the axial resolution was 500 μm or better up to 5 cm depth, and the lateral resolution was around 600 μm or better up to 5 cm depth.

3.3. Applications of TFPAI

3.3.1. Comparison between TFPAI and US in hemorrhage quantification

This study was designed to show the advantage of PA imaging using the TFPAI probe over conventional US imaging in quantifying the severity of a hemorrhage (located in the ventricular space or resulting from an intraparenchymal hemorrhage). Data analysis was performed on the signal from the 64th element of the transducer for both PA and US experiments. The peak amplitude of the signal was used to determine the concentration of blood. We calculated the range of samples in the time series within which the peak would be expected to be found using time-of-flight calculations. Each experiment was repeated 5 times and each time the data was acquired 100 times. A median value was identified for each experiment and the error bar shows the variation (that is, the full range of values found in all 5 experiments). Comparison of the US and PA readings for the hemorrhage-mimicking phantoms are given in Fig. 6. To simplify the analysis, the US and PA values were normalized to their minimum and maximum values in both graphs. In the case of the intraventricular hemorrhage mimicking phantom (Fig. 6d and f), it is evident that the PA signal exhibits a steep pattern of linear growth with increasing blood concentration, even from very low concentration samples (0.2%) whereas, the US signal is incapable of providing a meaningful pattern at this concentration (i.e., US cannot quantify low blood concentration hemorrhages). Only at concentrations around 6% or higher can US detect the presence of blood (still without quantification as shown in Fig. 6d). A similar pattern was seen in the intraparenchymal hemorrhage mimicking phantom (Fig. 6e and g) where TFPAI was able to detect and quantify blood concentration in tissue as low as 0.25%. By comparison, the US signal can detect presence of blood from 0.8% concentration (with a higher value than the 0% blood value). From 1.2%, US signal does increase monotonically. This demonstrates that unlike US, PA can quantify blood, even at low concentrations both in saline and in the brain tissue phantom. The standard approach for determining limit of detection (LOD) for PA and US cannot be determined analytically, because the calibration curves are nonlinear.

3.3.2. Ex-vivo hemorrhage detection

The experimental setup to determine the modeled hemorrhage location and size inside the sheep brain *ex-vivo* is provided in Fig. 7a. The data in Fig. 7f represents fluence decay at different depths of the brain tissue as a function of wavelength. The modeled hemorrhage size and location are determined by counting the number of pixels in the processed PA or US image after binarization (see the steps in Fig. 7b, detail of the steps is given in the figure caption) [89]. We analyzed hemorrhages of different sizes at a single depth (see Fig. 7c, e) and of the same size at different depths (see Fig. 7d, g). It is evident from Fig. 7e that the PA response has a strictly positive linear relationship with the increasing size of hemorrhage. The PA response compares favorably to the US response, which has higher standard deviations and a less linear response at the lower blood volumes/hemorrhage sizes.

To measure the fluence decay profile (see Fig. 7g insert), excised sheep brain tissue samples sliced with 0.5–3 cm thicknesses were used. An optical fiber bundle was placed on one side of the tissue samples, and an energy meter (with 1 cm^2 aperture) was placed on the other side (with its center aligned to the center of the optical fiber bundle) to measure the fluence. The fluence decay curve versus depth was created (see Fig. 7f insert). Spline interpolation was used to create the fluence decay profile. The fluence decay profile was then used to correct the PA image intensity values versus depth. This was accomplished by normalizing the fluence decay profile and then dividing the PA image pixel value by the corresponding depth-specific value from the normalized fluence decay profile. As shown in Fig. 7g, US was able to detect the model hemorrhages, but normalized average intensity values (representing hemorrhage size) varied widely (<0.5–1 a.u.) by depth. By contrast, fluence-compensated PA results showed less than 5% deviation (0.95–1 a.u.) over a depth of 0.5–2.5 cm.

3.3.3. Oxygen saturation measurement

A comparison between sO_2 readings determined by TFPAI and by BGA at different depths are provided in Fig. 8. The schematic and actual experimental setup are shown in Fig. 8a and b. Since a controlled sO_2 level cannot be achieved *ex-vivo*, we initially attempted to create a brain tissue solution and insert a blood vessel-mimicking tube filled with defibrinated sheep blood.

However, the bubbles in between the small pieces of brain tissue generated a high PA background signal (see Fig. 8c (i-iv)). Therefore, we utilized an intralipid-based brain tissue-mimicking phantom. The PA-based sO_2 values were calculated using Eq. (1) and Fig. 8d shows the sO_2 measurement at varying depths (0.5 – 5.0 cm) and O_2 concentrations (62–95%). Fig. 8e graphs sO_2 error by depth, (error bars represent the percent deviation from BGA measurements). Each point in the graph is the average of 100 PA signal acquisitions that were normalized by the corresponding laser energy. The extracted oxygenation results exhibit less than 3.2% deviation from the BGA measurements (i.e., “gold standard”).

3.3.4. Vessel rupture and vasogenic edema detection

Vessel Rupture Detection: Following the method described in Section 2.3.4, after Step 5, the phantom was imaged at 758 nm as shown in Fig. 9c(i). It is clear that the signal generated from blood made it difficult to localize the rupture. Changing the wavelength to 690 nm showed a reduction in blood signal (Fig. 9c(ii)). For the detection of rupture location, we slowly injected a 1 mg/mL MB (in saline) solution into the main vessel of the gelatin phantom (Step 6). We observed the movement of the dye in the vessel-like tube, and could readily detect the rupture location (Fig. 9c(iii)). This is because the molar extinction coefficient of MB is much higher at ~690 nm (Fig. 9d) than hemoglobin.

Vasogenic Edema Detection: The two inclusion phantom (edema + hemorrhage) was imaged over time as described in Section 2.3.4 at 690, 758 and 798 nm every 30 min for 3 h. The images were processed by spectral unmixing to determine relative concentration of MB in each inclusion. Results are shown in Fig. 9d(ii). The dye flowing through the edema bonded with the albumin leading to sustained high concentration levels, while unbound MB continued to diffuse through the hemorrhage model and hence a reduction in MB concentration was observed. This experiment establishes the proof of concept that the proposed TFPAI probe is capable of differentiating edema from hemorrhage by utilizing an exogenous contrast agent.

4. Discussion

To model potential applications of TFPAI in the NICU, several scenarios related to hemorrhage were studied through a series of in-vitro and *ex-vivo* experiments and the performance of TFPAI was evaluated. We showed TFPAI capabilities for identification of hemorrhage location and size, detection of blood in ventricular CSF, accurate determination of tissue oxygen saturation, and vessel rupture and edema localization.

An in-vitro model of a germinal matrix hemorrhage, i.e., a hemorrhage that originates due to the rupture of germinal matrix, with progression (Grade I and II) towards the lateral ventricles was replicated by diluting blood samples to different concentrations and TFPAI was able to detect and quantify a concentration as low as 0.2% blood, whereas US imaging could perhaps detect, but not quantify concentrations below 3% blood (Fig. 6d and f). In neonates, CSF has a total volume of 9–14 mL [91] which means TFPAI may be capable of detecting as low as 18 μL of blood mixed with CSF. In reality, CSF flows out of ventricles and a small, slow bleed into the ventricles often leads to no bleeding being observed in US images until the blood volume is greater than 5% of ventricular space. Further, we used a phantom consisting of a mixture of brain tissue and blood embedded in gelatin to mimic a severe hemorrhagic lesion (IVH causing ventriculomegaly, and intraparenchymal hemorrhage). A minimum concentration of 0.25% blood + tissue was successfully identified by the TFPAI system, in comparison to the minimum concentration of 1.2% detected by US (See Fig. 6e and g). In the future, we expect this ability to differentiate between blood and other materials will persist in-vivo.

Further characterization of TFPAI for detecting intracerebral hemorrhage was carried out *ex-vivo*. A blood clot mixed with brain tissue was differentiated from nearby healthy tissue. We showed that a hemorrhagic lesion with a minimum diameter of 1 mm (20 μL) at a depth of 2.5 cm can accurately be detected using TFPAI (see Fig. 7c). A linear fit model based on least square error demonstrated improved linearity between pixel areas and the modeled intracerebral hemorrhage size (injected blood volume) for PA (R^2: 0.98) as compared to US (R^2: 0.81) (see Fig. 7e). From a clinical point of view, the improved predictability of PA results could better quantify the amount of bleeding into the brain tissue and better determine hemorrhage location within the brain. The benefit of correctly identifying small concentrations of hemorrhage allows for earlier additional diagnostic and therapeutic interventions, which may reveal underlying medical issues, such as clotting factor disorders, vitamin K deficiency, thrombocytopenia, or other causes of hemorrhagic events so appropriate treatments can be initiated promptly to minimize the risk of future neurological complications. We observed US, at low concentrations, was not as quantifiable as PA (Fig. 7e). US was also shown to be not able to quantify hemorrhage volume (representing severity) at different depths (Fig. 7g). US shortcomings at hemorrhage characterization may mislead clinicians, causing less accurate diagnoses and potentially unnecessary interventions.

The TFPAI probe was tested in-vitro to evaluate its performance in terms of accuracy in measuring oxygen saturation by comparison with BGA results. We measured sO_2 values in an appropriate range (encompassing hypoxia and normoxia) up to 5 cm depth (see Fig. 8d). When compared to the gold standard BGA results, average error was around 2%. We tested the accuracy of the TFPAI probe for the measurement of sO_2 at different depths (see Fig. 8e). Unlike pulse oximetry (which collects information from the entire tissue sampled), TFPAI quantifies oxygenation at specific locations and depths, which could provide important diagnostic information. Relative accuracy between TFPAI and pulse oximetry cannot be determined, however, from our strictly in-vitro results. [92–94]. Assessment of cerebral tissue hypoxia in neonates is extremely useful in the clinical setting, and could become an important application of TFPAI. Acute and chronic episodes of hypoxia can lead to damage of BBB through the inflammatory response, and may cause disability or death in neonates [95]. Functional MRI is currently the method of choice for investigating neonatal hypoxic and ischemic events, however, this is not feasible when the neonate is in a clinically unstable condition [96,97].

Vasogenic edema following hemorrhage or ischemia/reperfusion injury (vessel rupture) is currently detected using contrast-enhanced MRI [98]. In this study, we demonstrated that the extravasation of albumin (modeling blood plasma proteins, the main component in edema) can be detected using the exogenous contrast agent MB (see Fig. 9d(ii)).

We also demonstrated the capability of TFPAI for the identification of the location of a vessel rupture (see Fig. 9c (i-iii)). Other organic and inorganic FDA-approved optical contrast agents can be utilized [99]. Taken together, these capabilities suggest TFPAI could potentially enable earlier detection of vascular dysfunction and bleeding in the neonatal brain.

This study was focused on demonstrating the potential applications of TFPAI and the evaluation of its performance in an environment that models transfontanelle imaging in an actual neonatal head. However, there are several limitations observed in terms of the design and probe application: (1) a more optimum fiber bundle configuration can be developed (e.g. see [100,101]); (2) a more sophisticated illumination scheme could be found; (3) higher sensitivity transducers could be used; and (4) most importantly, the method must be tested in-vivo. During the design phase, a major concern was the limited fontanelle area that eventually posed two constraints: (1) not able to maximize the number of rows of optical fibers since it would not be beneficial if part of the light is outside the fontanelle area and (2) not able to increase the optical energy due to potential tissue damage. The laser itself is non-ionizing, but the primary concern of this modality is possible effects on the skin of the newborn. For in-vivo measurement, a continuous temperature regulation mechanism could be introduced to suppress temperature build-up (without inducing hypothermia). Limited optical energy and area of illumination adversely impact the PA signal and image quality. To increase penetration depth and extract structural components located deep inside the brain, advanced signal enhancement and image reconstruction algorithms should be implemented. Based on the in-vitro and *ex-vivo* studies included in [102] and this report, it is suggested that TFPAI can potentially detect and quantify earlier-stage hemorrhages (i.e., lower concentrations of blood in CSF and smaller volumes of intracerebral and subependymal hemorrhages) than US imaging. However, this statement has only been studied under in-vitro and *ex-vivo* conditions and must be further evaluated in-vivo for translation of TFPAI to the clinic.

After qualifying the system in-vivo, the applications of TFPAI can potentially be expanded to diagnosis of ischemic events and ischemia-reperfusion injuries of neonatal brain. For example, using a neonatal porcine model of hypoxia-ischemia brain injury, Kang, et al. [103] has demonstrated a robust linear correlation between PAI-based measurements of sagittal sinus sO_2 with those measured directly by blood sampling over a wide range of conditions. In another study by the same group [104], it has been demonstrated in neonatal piglets that transcranial PA neuroimaging can be used to detect a regional thrombotic stroke in the cerebral cortex and that the oxygen saturation metric can be used alone to identify regional stroke lesions.

5. Conclusion

We have demonstrated some potential capabilities of TFPAI for diagnosing brain injuries in neonates through a series of in-vitro and *ex-vivo* experiments. TFPAI requires many more optimizations and evaluations in-vivo to be established as a neuroimaging modality in the NICU. Based on the results we have presented, we expect that TFPAI would provide complementary information for existing TFUSI systems that are routinely used in the NICU and also be able to map brain perfusion similar to fMRI with no need for sedation, radiation, or radionuclides. The proposed TFPAI technology is intended as a point-of-care non-invasive diagnostic device, which can be utilized immediately and repeatedly after birth. While the cost of building a TFPAI system for clinical use would be higher than off-the-shelf TFUSI, the estimated cost of a TFPAI procedure will be similar to the cost of a TFUSI procedure and holds the promise of reducing preventable complications due to brain injury by identifying various intracerebral events earlier.

Funding

This work was supported by the National Institutes of Health R01EB027769-01, and R01EB028661-01.

CRediT authorship contribution statement

Rayyan Manwar: Conceptualization, Data curation, Formal analysis, Methodology, Software, Validation, Writing – original draft, Writing – review & editing. **Karl Kratkiewicz:** Data curation, Formal analysis, Methodology, Validation, Writing – original draft. **Sadreddin Mahmoodkalayeh:** Data curation, Software, Writing – original draft. **Ali Hariri:** Conceptualization, Data curation, Formal analysis. **Christos Papadelis:** Review & editing. **Anne Hansen:** Writing – review & editing. **De-Ann Pillers:** Writing – review & editing. **Juri Gelovani:** Conceptualization, Formal analysis, Methodology, Resources, Supervision, Validation, Writing – review & editing. **Kamran Avanaki:** Conceptualization, Data curation, Formal analysis, Funding acquisition, Methodology, Project administration, Resources, Software, Supervision, Validation, Writing – original draft, Writing –review & editing.

Declaration of Competing Interest

The authors declare the following financial interests/personal relationships which may be considered as potential competing interests: Kamran Avanaki reports financial support was provided by National Institutes of Health. Kamran Avanaki has patent issued to Wayne State University. Juri G. Gelovani has patent issued to Wayne State University.

Data Availability

Data will be made available on request.

Appendix A. Supporting information

Supplementary data associated with this article can be found in the online version at doi:10.1016/j.pacs.2023.100538.

References

[1] Melonie Heron, Sutton, D. Paul, Jiaquan Xu, Stephanie J. Ventura, Donna M. Strobino, Bernard Guyer, Annual summary of vital statistics: 2007, Pediatrics 125 (1) (2010) 4–15.
[2] Tim Lekic, Damon Klebe, Poblete, R. Roy, Krafft, B.Rolland Paul, Tang William, Jiping, John H Zhang, Neonatal brain hemorrhage (NBH) of prematurity: translational mechanisms of the vascular-neural network, Curr. Med. Chem. 22 (10) (2015) 1214–1238.
[3] Griffiths, Ruth, The abilities of babies: a study in mental measurement. 1954.
[4] D.M. Luiz, C.D. Foxcroft, R. Stewart, The construct validity of the Griffiths Scales of Mental Development, Child.: Care Health Dev. 27 (1) (2001) 73–83.
[5] Levene M, Intracranial haemorrhage at term, in: R. JM (Ed.), Roberton's Textbook of Neonatology, fourth ed., Elsevier, Philadelphia, 2005.
[6] Richard G. Perrin, Rutka, T. James, Drake, M. James, Hal Meltzer, Jonathan Hellman, Venita Jay, Harold J. Hoffman, Robin P. Humphreys, Management and outcomes of posterior fossa subdural hematomas in neonates, Neurosurgery 40 (6) (1997) 1190–1200.
[7] Rooij Van, G.M. Linda, Toet, C. Mona, Rademaker, M.A. Karin, Groenendaal, Floris, De Vries, S. Linda, Cardiac arrhythmias in neonates receiving lidocaine as anticonvulsive treatment, Eur. J. Pediatr. 163 (11) (2004) 637–641.
[8] Terry Morgan, Jamie McDonald, Christina Anderson, Magdy Ismail, Franklin Miller, Rong Mao, Ashima Madan, Patrick Barnes, Louanne Hudgins, Melanie Manning, Intracranial hemorrhage in infants and children with hereditary hemorrhagic telangiectasia (Osler-Weber-Rendu syndrome). Pediatrics 109 (1) (2002) p. e12-e12.
[9] Michelle J.K. Osterman, Kenneth D. Kochanek, Marian F. MacDorman, Donna M. Strobino, Bernard Guyer, Annual summary of vital statistics: 2012–2013, Pediatrics (2015) p. peds. 2015-0434.
[10] Lu-Ann Papile, Jerome Burstein, Rochelle Burstein, Herbert Koffler, Incidence and evolution of subependymal and intraventricular hemorrhage: a study of infants with birth weights less than 1,500 gm, J. Pediatr. 92 (4) (1978) 529–534.
[11] Alex Tsiantos, Lars Victorin, J.P. Relier, Norman Dyer, Hakan Sundell, A.B. Brill, Mildred Stahlman, Intracranial hemorrhage in the prematurely born infant: Timing of clots and evaluation of clinical signs and symptoms, J. Pediatr. 85 (6) (1974) 854–859.

[12] Annemieke J. Brouwer, Floris Groenendaal, Corine Koopman, Rutger-Jan A. Nievelstein, Sen K. Han, Linda S. de Vries, Intracranial hemorrhage in full-term newborns: a hospital-based cohort study. Neuroradiology 52 (6) (2010) 567–576.

[13] Hannah C. Glass, Costarino, T. Andrew, Stephen A. Stayer, Claire Brett, Franklyn Cladis, Peter J. Davis, Outcomes for extremely premature infants. Anesth. Analg. 120 (6) (2015) 1337.

[14] John D. Lantos, Diane S. Lauderdale, What is behind the rising rates of preterm birth in the United States? Rambam Maimonides Med. J. 2 (2011) 4.

[15] Surya N. Gupta, Amer M. Kechli, Uday S. Kanamalla, Intracranial hemorrhage in term newborns: management and outcomes. Pediatr. Neurol. 40 (1) (2009) 1–12.

[16] Mei-Chen Ou-Yang, Chung-Bin Huang, Hsin-Chun Huang, Mei-Yung Chung, Chih-Cheng Chen, Feng-Shun Chen, Pei-Hsin Chao, I.-Lun Chen, Mei-Hui Ou-Yang, Chieh-An Liu, Clinical manifestations of symptomatic intracranial hemorrhage in term neonates: 18 years of experience in a medical center, Pediatr. Neonatol. 51 (4) (2010) 208–213.

[17] Ann C. McKee, Daniel H. Daneshvar, *The Neuropathology of Traumatic Brain Injury*, in *Handbook of Clinical Neurology*, Elsevier, 2015, pp. 45–66.

[18] Rita de C.ássia Almeida Vieira, Wellingson Silva Paiva, Daniel Vieira de Oliveira, Manoel Jacobsen Teixeira, Almir Ferreira de Andrade, Regina M.árcia Cardoso de Sousa, Diffuse axonal injury: epidemiology, outcome and associated risk factors, Front. Neurol. 7 (2016) 178.

[19] Tim Lekic, Damon Klebe, Roy Poblete, Paul R. Krafft, William B. Rolland, Jiping Tang, John H. Zhang, Neonatal brain hemorrhage (NBH) of prematurity: translational mechanisms of the vascular-neural network, Curr. Med. Chem. 22 (10) (2015) 1214–1238.

[20] J.R. Little, G.A. Blomquist, R. Ethier, Intraventricular hemorrhage in adults, Surg. Neurol. 8 (3) (1977) 143–149.

[21] Terrie E. Inder, Perlman, M. Jeffrey, Joseph J. Volpe, Intracranial hemorrhage: subdural, subarachnoid, intraventricular (term infant). *Miscellaneous*, in *Volpe's Neurology of the Newborn*, *Sixth ed.*, Elsevier, 2018, pp. 593–622, e7.

[22] Ai. Peng Tan, Patricia Svrckova, Frances Cowan, Wui Khean Chong, Kshitij Mankad, Intracranial hemorrhage in neonates: a review of etiologies, patterns and predicted clinical outcomes, Eur. J. Paediatr. Neurol. (2018).

[23] Erika Uehara, Hiro Nakao, Yusuke Tsumura, Hisaya Nakadate, Shoichiro Amari, Hideshi Fujinaga, Yoshiyuki Tsutsumi, Dongchon Kang, Shouichi Ohga, Akira Ishiguro, Slow elevation in protein C activity without a PROC mutation in a neonate with intracranial hemorrhage, AJP Rep. 8 (2) (2018), e68.

[24] Joseph J. Volpe, Neurology of the Newborn E-Book, Elsevier Health Sciences, 2008.

[25] Susan C. Carson, Barbara S. Hertzberg, James D. Bowie, Peter C. Burger, Value of sonography in the diagnosis of intracranial hemorrhage and periventricular leukomalacia: a postmortem study of 35 cases, Am. J. Neuroradiol. 11 (4) (1990) 677–683.

[26] R. Llorens-Salvador, A. Moreno-Flores, The ABCs of transfontanellar ultrasound and more, Radiologia 58 (2016) 129–141.

[27] K.C. Eze, S.U. Enukegwu, Transfontanelle ultrasonography of infant brain: analysis of findings in 114 patients in Benin City, *Niger.* Niger. J. Clin. Pract. 13 (2010) 2.

[28] Terrie E. Inder, de Vries, S. Linda, Ferriero, M. Donna, P.Ellen Grant, Laura R. Ment, Steven P. Miller, Joseph J. Volpe, Neuroimaging of the preterm brain: review and recommendations, J. Pediatr. 237 (2021) 276–287, e4.

[29] Annemarie Plaisier, Raets, M.A. Marlou, Ecury-Goossen, M. Ginette, Paul Govaert, Monique Feijen-Roon, Irwin K.M. Reiss, Liesbeth S. Smit, Maarten H. Lequin, Jeroen Dudink, Serial cranial ultrasonography or early MRI for detecting preterm brain injury? Arch. Dis. Child. -Fetal Neonatal Ed. 100 (4) (2015) F293–F300.

[30] Ivan L. Hand, Renée A. Shellhaas, Sarah S. Milla, James J. Cummings, Ira S. Adams-Chapman, Susan Wright Aucott, Jay P. Goldsmith, David Alan Kaufman, Camilia Rivera Martin, Karen M. Puopolo, Routine neuroimaging of the preterm brain. Pediatrics 146 (2020) 5.

[31] Rayyan Manwar, Md. Tarikul Islam, Seyed Mohsen Ranjbaran, Kamran Avanaki, Transfontanelle photoacoustic imaging: ultrasound transducer selection analysis, Biomed. Opt. Express 13 (2) (2022) 676–693.

[32] Majid Mirmiran, Barnes, D. Patrick, *Neonatal brain magnetic resonance imaging before discharge is better than serial cranial ultrasound in predicting cerebral palsy in very low birth weight preterm infants*, Pediatrics 114 (4) (2004) 992–998.

[33] Brigitte Vollmer, Simon Roth, Jenny Baudin, Ann L. Stewart, Brian G.R. Neville, John S. Wyatt, Predictors of long-term outcome in very preterm infants: gestational age versus neonatal cranial ultrasound, Pediatrics 112 (5) (2003) 1108–1114.

[34] Shadi N. Malaeb, Meltem Izzetoglu, Jane McGowan, Maria Delivoria-Papadopoulos, Noninvasive monitoring of brain edema after hypoxia in newborn piglets, Pediatr. Res. 83 (2) (2018) 484.

[35] Joseph J. Volpe, Peter Herscovitch, Jeffrey M. Perlman, Katherine L. Kreusser, Marcus E. Raichle, Positron emmission tomography in the asphyxiated term newborn: parasagittal impairment of cerebral blood flow, Ann. Neurol. 17 (3) (1985) 287–296.

[36] R.Whit Hall, Rolla M. Shbarou, Drugs of choice for sedation and analgesia in the NICU, Clin. Perinatol. 36 (1) (2009) 15–26.

[37] Jean A. Tkach, Stephanie L. Merhar, Beth M. Kline-Fath, Ronald G. Pratt, Wolfgang M. Loew, Barret R. Daniels, Randy O. Giaquinto, Mantosh S. Rattan, Blaise V. Jones, Michael D. Taylor, Janice M. Tiefermann, Lisa M. Tully, E. Colleen Murphy, Rachel N. Wolf-Severs, Angela A. LaRuffa, Charles L. Dumoulin, MRI in the neonatal ICU: initial experience using a small-footprint 1.5-T system, Am. J. Roentgenol. 202 (1) (2013) W95–W105.

[38] H.U. Bucher, A.D. Edwards, A.E. Lipp, G. Duc, Comparison between near infrared spectroscopy and 133Xenon clearance for estimation of cerebral blood flow in critically ill preterm infants, Pediatr. Res. 33 (1993) 56.

[39] A.D. Edwards, Clare Richardson, M. Cope, J.S. Wyatt, D.T. Delpy, E.O. R. Reynolds, Cotside measurement of cerebral blood flow in ill newborn infants by near infrared spectroscopy, Lancet 332 (8614) (1988) 770–771.

[40] P.Gopinath Shankar, Claudia S. Robertson, Charles F. Contant, Raj K. Narayan, Robert G. Grossman, Britton Chance, Early detection of delayed traumatic intracranial hematomas using near-infrared spectroscopy, J. Neurosurg. 83 (3) (1995) 438–444.

[41] Richard N. Aslin, Jacques Mehler, Near-infrared spectroscopy for functional studies of brain activity in human infants: promise. prospects, and challenges, SPIE,, 2005.

[42] C. Demene, J. Baranger, M. Bernal, C. Delanoe, S. Auvin, V. Biran, M. Alison, J. Mairesse, E. Harribaud, M. Pernot, M. Tanter, O. Baud, Functional ultrasound imaging of brain activity in human newborns, Sci. Transl. Med 9 (411) (2017).

[43] Moein Mozaffarzadeh, Ali Mahloojifar, Mahdi Orooji, Saba Adabi, Mohammadreza Nasiriavanaki, Double-stage delay multiply and sum beamforming algorithm: application to linear-array photoacoustic imaging. IEEE Trans. Biomed. Eng. 65 (1) (2017) 31–42.

[44] Hariri, Ali, Omidi, Parsa, and Nasiriavanaki, Mohammadreza. Resting-state functional connectivity measurement in the mouse brain using a low cost photoacoustic computed tomography. in Laser Science. 2016. Optical Society of America.

[45] Bruno-F.élix Osmanski, Sophie Pezet, Ana Ricobaraza, Zsolt Lenkei, Mickael Tanter, Functional ultrasound imaging of intrinsic connectivity in the living rat brain with high spatiotemporal resolution, Nat. Commun. 5 (2014) 5023.

[46] Sadreddin Mahmoodkalayeh, Karl Kratkiewicz, Rayyan Manwar, Shahbazi, Ansari Meysam, Ali Mohammad, Girija Natarajan, Eishi Asano, Kamran Avanaki, Wavelength and pulse energy optimization for detecting hypoxia in photoacoustic imaging of the neonatal brain: a simulation study, Biomed. Opt. Express 12 (12) (2021) 7458–7477.

[47] Rayyan Manwar, Karl Kratkiewicz, Kamran Avanaki, Investigation of the effect of the skull in transcranial photoacoustic imaging: a preliminary ex vivo study, Sensors 20 (15) (2020) 4189.

[48] Rayyan Manwar, Laura S. McGuire, Md Islam, Anthony Shoo, Fady T. Charbel, De-Ann M. Pillers, Kamran Avanaki, Transfontanelle photoacoustic imaging for in-vivo cerebral oxygenation measurement, Sci. Rep. 12 (1) (2022) 1–7.

[49] James I. Matchynski, Rayyan Manwar, Karl J. Kratkiewicz, Rajtarun Madangopal, Veronica A. Lennon, Kassem M. Makki, Abbey L. Reppen, Alexander R. Woznicki, Bruce T. Hope, Shane A. Perrine, Direct measurement of neuronal ensemble activity using photoacoustic imaging in the stimulated Fos-LacZ transgenic rat brain: a proof-of-principle study, Photoacoustics 24 (2021), 100297.

[50] Sadreddin Mahmoodkalayeh, Mehrdad Zarei, Mohammad Ali Ansari, Karl Kratkiewicz, Mohsen Ranjbaran, Rayyan Manwar, Kamran Avanaki, Improving vascular imaging with co-planar mutually guided photoacoustic and diffuse optical tomography: a simulation study, Biomed. Opt. Express 11 (8) (2020) 4333–4347.

[51] Leila Mohammadi, Hamid Behnam, Jahan Tavakkoli, Kamran Avanaki, Skull acoustic aberration correction in photoacoustic microscopy using a vector space similarity model: a proof-of-concept simulation study, Biomed. Opt. Express 11 (10) (2020) 5542–5556.

[52] Lihong V. Wang, Tutorial on photoacoustic microscopy and computed tomography, IEEE J. Sel. Top. Quantum Electron. 14 (1) (2008) 171–179.

[53] Joon-Mo Yang, Christopher Favazza, Ruimin Chen, Junjie Yao, Xin Cai, Konstantin Maslov, Qifa Zhou, K.Kirk Shung, Lihong V. Wang, Simultaneous functional photoacoustic and ultrasonic endoscopy of internal organs in vivo, Nat. Med. 18 (8) (2012) 1297.

[54] John Gamelin, Anastasios Maurudis, Andres Aguirre, Fei Huang, Puyun Guo, Lihong V. Wang, Quing Zhu, A real-time photoacoustic tomography system for small animals, Opt. Express 17 (13) (2009) 10489–10498.

[55] Junjie Yao, Jun Xia, Maslov, I. Konstantin, Mohammadreza Nasiriavanaki, Vassiliy Tsytsarev, Alexei V. Demchenko, Lihong V. Wang, Noninvasive photoacoustic computed tomography of mouse brain metabolism in vivo, Neuroimage 64 (2013) 257–266.

[56] Avanaki, Kamran and Gelovani, Juri G., Ultrasound and multispectral photoacoustic systems and methods for brain and spinal cord imaging through acoustic windows. 2020, Google Patents.

[57] Mohammadreza Nasiriavanaki, Jun Xia, Hanlin Wan, Adam Quentin Bauer, Joseph P. Culver, Lihong V. Wang, High-resolution photoacoustic tomography of resting-state functional connectivity in the mouse brain, Proc. Natl. Acad. Sci. USA 111 (1) (2014) 21–26.

[58] Yoko Hoshi, Functional near-infrared optical imaging: utility and limitations in human brain mapping, Psychophysiology 40 (4) (2003) 511–520.

[59] Arlene Duncan, Judith H. Meek, Matthew Clemence, Clare E. Elwell, Penny Fallon, Lidia Tyszczuk, Mark Cope, David T. Delpy, Measurement of cranial optical path length as a function of age using phase resolved near infrared spectroscopy, Pediatr. Res. 39 (5) (1996) 889–894.

[60] Adam J. Wolfberg, Adré J. du Plessis, Near-infrared spectroscopy in the fetus and neonate, Clin. Perinatol. 33 (3) (2006) 707–728.

[61] Zachary A. Vesoulis, Mintzer, P. Jonathan, Valerie Y. Chock, Neonatal NIRS monitoring: recommendations for data capture and review of analytics, J. Perinatol. 41 (4) (2021) 675–688.

[62] S.E. Nicklin, I.A.A. Hassan, Y.A. Wickramasinghe, S.A. Spencer, The light still shines, but not that brightly? The current status of perinatal near infrared spectroscopy, Arch. Dis. Child. -Fetal Neonatal Ed. 88 (4) (2003) F263–F268.

[63] America, Laser Institute of, American National Standard for Safe Use of Lasers ANSI Z136. 1–2014. 2014, American National Standards Institute, Inc Washington, DC.

[64] Qianqian Fang, David A. Boas, Monte Carlo simulation of photon migration in 3D turbid media accelerated by graphics processing units, Opt. Express 17 (22) (2009) 20178–20190.

[65] A.N. Bashkatov, E.A. Genina, V.I. Kochubey, V.V. Tuchin, Optical properties of human skin, subcutaneous and mucous tissues in the wavelength range from 400 to 2000 nm, J. Phys. D: Appl. Phys. 38 (15) (2005) 2543.

[66] Nadya Ugryumova, Stephen John Matcher, Don P. Attenburrow, Measurement of bone mineral density via light scattering. Phys. Med. Biol. 49 (3) (2004) 469.

[67] Karl Kratkiewicz, Rayyan Manwar, Yang Zhou, Moein Mozaffarzadeh, Kamran Avanaki, Technical considerations in the Verasonics research ultrasound platform for developing a photoacoustic imaging system, Biomed. Opt. Express 12 (2) (2021) 1050–1084.

[68] Thomas Kirchner, Franz Sattler, Janek Gröhl, Lena Maier-Hein, Signed real-time delay multiply and sum beamforming for multispectral photoacoustic imaging, J. Imaging 4 (10) (2018) 121.

[69] E.A. Ginzel, R.K. Ginzel, Ginzel Brothers, *Ultrasonic Properties of a New Low Attenuation Dry Couplant Elastomer.*, Ginzel Brothers & Associates Ltd, 1994.

[70] Nyholt, John and Langlois, Gary N., Dry-coupled permanently installed ultrasonic sensor linear array. 2013, Google Patents.

[71] Yochev, Bogomil, Kutzarov, Svetoslav, Ganchev, Damyan, and Staykov, Krasimir. Investigation of ultrasonic properties of hydrophilic polymers for dry-coupled inspection. in Proceedings of the European Conference on Non-Destructive Testing, Berlin, Germany. 2006. Citeseer.

[72] Rayyan Manwar, Loïc Saint-Martin, Kamran Avanaki, Couplants in acoustic biosensing systems, Chemosensors 10 (5) (2022) 181.

[73] Najme Meimani, Nina Abani, Juri Gelovani, Mohammad R.N. Avanaki, A numerical analysis of a semi-dry coupling configuration in photoacoustic computed tomography for infant brain imaging, Photoacoustics 7 (2017) 27–35.

[74] Carina Mallard, Zinaida S. Vexler, Modeling ischemia in the immature brain: how translational are animal models? Stroke 46 (10) (2015) 3006–3011.

[75] David K. Stevenson, William E. Benitz, Philip Sunshine, Susan R. Hintz, Maurice L. Druzin, Fetal and Neonatal Brain Injury, Cambridge University Press, 2017.

[76] Chris E. Williams, Gunn, J. Alistair, Carina Mallard, Peter D. Gluckman, Outcome after ischemia in the developing sheep brain: an electroencephalographic and histological study, Ann. Neurol. 31 (1) (1992) 14–21.

[77] Xueding Wang, Xueyi Xie, Geng Ku, Lihong V. Wang, George Stoica, Noninvasive imaging of hemoglobin concentration and oxygenation in the rat brain using high-resolution photoacoustic tomography, J. Biomed. Opt. 11 (2) (2006), 024015.

[78] Xueding Wang, Chamberland, L. David, Guohua Xi, Noninvasive reflection mode photoacoustic imaging through infant skull toward imaging of neonatal brains, J. Neurosci. Methods 168 (2) (2008) 412–421.

[79] A.L. Bendinger, C. Glowa, J. Peter, C.P. Karger, Photoacoustic imaging to assess pixel-based sO2 distributions in experimental prostate tumors, J. Biomed. Opt. 23 (3) (2018) 1–11.

[80] Emma Brown, Joanna Brunker, Sarah E. Bohndiek, Photoacoustic imaging as a tool to probe the tumour microenvironment, Dis. Models Mech. 12 (7) (2019).

[81] Fei Cao, Zhihai Qiu, Huanhao Li, Puxiang Lai, Photoacoustic imaging in oxygen detection, Appl. Sci. 7 (12) (2017) 1262.

[82] Wei Shen, Jia-Hua Pan, Wei-Dong Chen, Comparison of transcranial ultrasound and cranial MRI in evaluations of brain injuries from neonatal asphyxia, Int. J. Clin. Exp. Med. 8 (10) (2015) 18319.

[83] Roy DiVittorio, Bluth, I. Edward, Michael A. Sullivan, Deep vein thrombosis: diagnosis of a comon clinical problem, Ochsner J. 4 (1) (2002) 14–17.

[84] Gita Yashwantrao Karande, Hedgire, S. Sandeep, Yadiel Sanchez, Vinit Baliyan, Vishala Mishra, Suvranu Ganguli, Anand M. Prabhakar, Advanced imaging in acute and chronic deep vein thrombosis, Cardiovasc. Diagn. Ther. 6 (6) (2016) 493.

[85] Paulo Roberto Barbosa Evora, Andrea Carla Celotto, Agnes Afrodite Sumarelli Albuquerque, Patricia Martinez Évora, *Methylene Blue in Children and Neonates*, in *Vasoplegic Endothelial Dysfunction: Circulatory Shock and Methylene Blue*, Springer, 2021, pp. 75–80.

[86] E.J. Kang, S. Major, D. Jorks, C. Reiffurth, N. Offenhauser, A. Friedman, J. P. Dreier, Blood–brain barrier opening to large molecules does not imply blood–brain barrier opening to small ions, Neurobiol. Dis. 52 (2013) 204–218.

[87] Norman R. Saunders, Dziegielewska, M. Katarzyna, Kjeld Møllgård, Mark D. Habgood, Markers for blood-brain barrier integrity: how appropriate is Evans blue in the twenty-first century and what are the alternatives? Front. Neurosci. 9 (2015) 385.

[88] Gerard C. Van Rhoon, Theodoros Samaras, Pavel S. Yarmolenko, Mark W. Dewhirst, Esra Neufeld, Niels Kuster, CEM43° C thermal dose thresholds: a potential guide for magnetic resonance radiofrequency exposure levels? Eur. Radiol. 23 (8) (2013) 2215–2227.

[89] Rayyan Manwar, Md. Tarikul Islam, Anthony Shoo, De-Ann Pillers, Kamran Avanaki, Development of ex-vivo brain hemorrhage phantom for photoacoustic imaging, J. Biophotonics (2023), e202200313.

[90] Tzoumas, Stratis, Ntziachristos, Vasilis %J Philosophical Transactions of the Royal Society A: Mathematical, Physical, and Sciences, Engineering, Spectral unmixing techniques for optoacoustic imaging of tissue pathophysiology. 2017. 375(2107): p. 20170262.

[91] Zheng Lu, Jintao He, Yaxiong Yu, Zhicen Li, Zhi Li, Jian Gong, Measurement of lateral ventricle volume of normal infant based on magnetic resonance imaging, Chin. Neurosurg. J. 5 (02) (2019) 65–70.

[92] Dirk Wackernagel, Mats Blennow, Ann Hellström, Accuracy of pulse oximetry in preterm and term infants is insufficient to determine arterial oxygen saturation and tension, Acta Paediatr. 109 (11) (2020) 2251–2257.

[93] Thomas Edward Bachman, Christopher J.L. Newth, Patrick A. Ross, Narayan P. Iyer, Robinder G. Khemani, Characterization of the bias between oxygen saturation measured by pulse oximetry and calculated by an arterial blood gas analyzer in critically ill neonates, Lékař a Tech. -Clin. Technol. 47 (4) (2017) 130–134.

[94] Shyang-Yun Pamela K. Shiao, Ching-Nan Ou, Validation of oxygen saturation monitoring in neonates, Am. J. Crit. Care 16 (2) (2007) 168–178.

[95] Wei Ling Amelia Lee, Adina T. Michael-Titus, Divyen K. Shah, Hypoxic-ischaemic encephalopathy and the blood-brain barrier in neonates, Dev. Neurosci. 39 (1–4) (2017) 49–58.

[96] S.Todd Sorokan, Ann L. Jefferies, Steven P. Miller, Imaging the term neonatal brain, Paediatr. Child Health 23 (5) (2018) 322–328.

[97] Christopher D. Smyser, Jeffrey J. Neil, Use of resting-state functional MRI to study brain development and injury in neonates. Seminars in Perinatology, Elsevier, 2015.

[98] Jie Pan, Angelos-Aristeidis Konstas, Brian Bateman, Girolamo A. Ortolano, John Pile-Spellman, Reperfusion injury following cerebral ischemia: pathophysiology, MR imaging, and potential therapies, Neuroradiology 49 (2) (2007) 93–102.

[99] Jean-Christophe Ferré, Mark S. Shiroishi, Meng Law, Advanced techniques using contrast media in neuroimaging, Magn. Reson. Imaging Clin. 20 (4) (2012) 699–713.

[100] Rayyan Manwar, Juliana Benavides Lara, Ravi Prakash, Seyed Mohsen Ranjbaran, Kamran Avanaki, Randomized multi-angle illumination for improved linear array photoacoustic computed tomography in brain, J. Biophotonics (2022), e202200016.

[101] Rayyan Manwar, Xin Li, Sadreddin Mahmoodkalayeh, Eishi Asano, Dongxiao Zhu, Kamran Avanaki, Deep learning protocol for improved photoacoustic brain imaging, J. Biophotonics 13 (10) (2020), e202000212.

[102] Manwar, Rayyan, Gelovani, Juri G., and Avanaki, Kamran, *Bilirubin-Biliverdin Concentration Measurement using Photoacoustic Spectroscopic Analysis for Determining Hemorrhage Age*. Journal of Biophotonics: p. e202200316.

[103] Jeeun Kang, Emad M. Boctor, Shawn Adams, Ewa Kulikowicz, Haichong K. Zhang, Raymond C. Koehler, Ernest M. Graham, Validation of noninvasive photoacoustic measurements of sagittal sinus oxyhemoglobin saturation in hypoxic neonatal piglets, J. Appl. Physiol. 125 (4) (2018) 983–989.

[104] Jeeun Kang, Xiuyun Liu, Suyi Cao, Steven R. Zeiler, Ernest M. Graham, Emad M. Boctor, Raymond C. Koehler, Transcranial photoacoustic characterization of neurovascular physiology during early-stage photothrombotic stroke in neonatal piglets in vivo, J. Neural Eng. 18 (6) (2022), 065001.

Rayyan Manwar received his PhD from University of Windsor, Windsor, Ontario in 2017. His bachelor's was in Electrical and Electronic Engineering from Islamic University of Technology (IUT), Bangladesh in 2011. Currently, he is a research specialist at OPIRA LAB, Biomedical Engineering Department at University of Illinois at Chicago. Previously, he was a post doctoral fellow in Bioengineering Department at Wayne State University, Detroit, MI. His research interests include MEMS based design, fabrication and characterization, photoacoustic and ultrasound imaging.

Karl Kratkiewicz is currently a Product Engineer in the semiconductor industry working on electron beam review tools. He earned his PhD in Biomedical Engineering in 2020 at Wayne State University, Detroit, Michigan. He graduated with an M.S. in Biomedical Engineering in 2018 from Wayne State University. He graduated summa cum laude with a B.S. in Biomedical Physics from Wayne State University's Honors College in 2017. His area of research included ultrasound tomography image reconstruction algorithms and multimodal (ultrasound/photoacoustic/elastography) imaging.

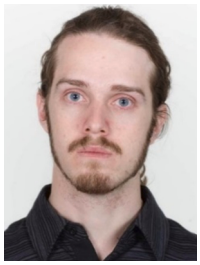

Sadreddin Mahmoodkalayeh received his M.S. in physics from Sharif University, Tehran, Iran in 2003. Graduated with PhD in Physics from Shahid Beheshti University, Tehran, Iran in 2020. His research field includes photoacoustic imaging, diffuse optical tomography.

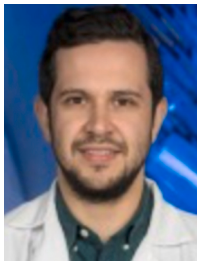

Ali Hariri received his PhD from the Department of Nanoengineering at UCSD. His research focused on developing, improving, and utilizing low fluence-based photoacoustic imaging systems. He worked on developing different configurations of photoacoustic imaging technique including computed tomography and microscopy (both acoustic and optical resolution). His LED-photoacoustic imaging characterization publication in 2018 is one of the most cited articles in Photoacoustic Journal, to date.

Christos Papadelis is currently the Director of Neuroscience Research at Cook Children's Health Care System, a Professor of Research in Bioengineering at University of Texas at Arlington, and a Professor of Pediatrics at Texas Christian University School of Medicine. Prior to this position, he was an Assistant Professor of Pediatrics at Harvard Medical School and Director of the Clinical Magnetoencephalography Program at Boston Children's Hospital. He received his Ph.D. from the Aristotle University of Thessaloniki, Greece, and worked as Postdoctoral Researcher in RIKEN Brain Science Institute, Japan, and University of Trento, Italy. His areas of expertise are the presurgical evaluation of children with drug resistant epilepsy and mapping of brain plasticity in infants and children with cerebral palsy.

Anne Hansen is an Associate Professor of Pediatrics at Harvard Medical School. She received her medical education at Harvard Medical School. She completed her pediatric residency and neonatology fellowship at Boston Children's Hospital. She is now the medical director of the Neonatal Intensive Care Unit, Associate Chief of the Division of Newborn Medicine and the Barry Family Research Chair at Boston Children's Hospital. Her research focuses on medical device development for newborns in both high and low resource settings.

De-Ann Pillers is the head of the Section of Neonatology at UI Health. In her role, she assures the continued success of clinical neonatology programs and supports the scholarly pursuit of excellence in newborn medicine.

Juri George Gelovani is a world-renown leader in molecular and functional imaging, and the founder of molecular-genetic and epigenetic imaging fields. He started his academic career at the University of Tartu, Estonia in 1989, then he joined Memorial Sloan-Kettering Cancer Center (New York, NY) in 1991 as a Postdoctoral Fellow; in 2003 joined the Univerisy of Texas MD Anderson Cancer Center (Houston, TX) as Full Professor, Deapartment Chair, and Imaging center Director; in 2012 moved to Wayne State University (WSU) and Karmanos Cancer Institute (Detroit, MI) as Department Chair, Imaging Program Leader, and Director of Engineering in Medicine. In 2020, he moved to the United Arab Emirates University, UAEU (Al Ain, UAE).

Kamran Avanaki is currently an Associate Professor of Biomedical Engineering Department at the University of Illinois in Chicago. Prior to this position, he was an Associate Professor of Biomedical Engineering Department at Wayne State University. He received his Ph.D. degree from the University of Kent, the United Kingdom with an Outstanding Achievement Honor in Medical Optical Imaging and Computing in 2012. His areas of expertise are design and development of photoacoustic imaging technology and optical coherence tomography for biomedical applications to solve critical problems in brain and skin imaging.